Constraining the Evolution of the Ionizing Background and the Epoch of Reionization with $z\sim 6$ Quasars II: A Sample of 19 Quasars^{1,2}

Xiaohui Fan³, Michael A. Strauss⁴, Robert H. Becker^{5,6}, Richard L. White⁷, James E. Gunn⁴, Gillian R. Knapp⁴, Gordon T. Richards^{4,8}, Donald P. Schneider⁹, J. Brinkmann¹⁰ and Masataka Fukugita¹¹

ABSTRACT

We study the evolution of the ionization state of the intergalactic medium (IGM) at the end of the reionization epoch using moderate resolution spectra of a sample of nineteen quasars at $5.74 < z_{\rm em} < 6.42$ discovered in the Sloan Digital Sky Survey. Three methods are used to trace IGM properties: (a) the evolution of the Gunn-Peterson (GP) optical depth in the Ly α , β , and γ transitions; (b) the distribution of lengths of dark absorption gaps, and (c) the size of HII regions around luminous quasars. Using this large sample, we find that the evolution of the ionization state of the IGM accelerated at z > 5.7: the GP optical depth evolution changes from $\tau_{\rm GP}^{\rm eff} \sim (1+z)^{4.3}$ to $(1+z)^{\gtrsim 11}$, and the average length of dark gaps with $\tau > 3.5$ increases from < 10 to > 80 comoving Mpc. The dispersion of IGM properties along different lines of sight also increases rapidly, implying fluctuations by a factor of $\gtrsim 4$ in the UV background at

¹Based on observations obtained with the Sloan Digital Sky Survey; at the W.M. Keck Observatory, which is operated as a scientific partnership among the California Institute of Technology, the University of California and the National Aeronautics and Space Administration, made possible by the generous financial support of the W.M. Keck Foundation, with the MMT Observatory, a joint facility of the University of Arizona and the Smithsonian Institution, and with the Kitt Peak National Observatory 4-meter Mayall Telescope.

²This paper is dedicated to the memory of John N. Bahcall.

³Steward Observatory, The University of Arizona, Tucson, AZ 85721; fan@as.arizona.edu

⁴Princeton University Observatory, Princeton, NJ 08544

⁵Physics Department, University of California, Davis, CA 95616

⁶IGPP/Lawrence Livermore National Laboratory, Livermore, CA 94550

⁷Space Telescope Science Institute, Baltimore, MD 21218

⁸Department of Physics and Astronomy, The Johns Hopkins University, Baltimore, MD 21218

⁹Department of Astronomy and Astrophysics, The Pennsylvania State University, University Park, PA 16802

¹⁰Apache Point Observatory, P. O. Box 59, Sunspot, NM 88349-0059

¹¹Institute for Cosmic Ray Research, University of Tokyo, Midori, Tanashi, Tokyo 188-8502, Japan

z>6, when the mean free path of UV photons is comparable to the correlation length of the star forming galaxies that are thought to have caused reionization. The mean length of dark gaps shows the most dramatic increase at $z\sim6$, as well as the largest line-of-sight variations. We suggest using dark gap statistics as a powerful probe of the ionization state of the IGM at yet higher redshift. The sizes of HII regions around luminous quasars decrease rapidly towards higher redshift, suggesting that the neutral fraction of the IGM has increased by a factor of $\gtrsim 10$ from z=5.7 to 6.4, consistent with the value derived from the GP optical depth. The mass-averaged neutral fraction is 1-4% at $z\sim6.2$ based on the GP optical depth and HII region size measurements. The observations suggest that $z\sim6$ is the end of the overlapping stage of reionization, and are inconsistent with a mostly neutral IGM at $z\sim6$, as indicated by the finite length of dark absorption gaps.

Subject headings: quasars: general; cosmology: observations; quasars: absorption lines; intergalactic medium

1. Introduction

After the recombination epoch at $z \sim 1100$, the universe became mostly neutral, until the first generation of stars and quasars reionized the intergalactic medium (IGM) and ended the cosmic "dark ages" (e.g., Rees 1998). Cosmological models predict reionization at redshifts between 6 and 20 (e.g., Gnedin & Ostriker 1997, Gnedin 2000, 2004, Ciardi et al. 2001, Benson et al. 2001, Razoumov et al. 2002, Cen 2003a,b, Ciardi, Ferrara & White 2003, Haiman & Holder 2003, Wyithe & Loeb 2003a, Somerville et al. 2003, Choudhury & Ferrara 2005). When and how the universe reionized remains one of the fundamental questions of modern cosmology (for reviews of theoretical models, see Barkana & Loeb 2001, Loeb & Barkana 2001, and Ciardi & Ferrara 2005).

The last few years have witnessed the first direct observational constraints on the history of reionization. Lack of complete Gunn-Peterson (GP, 1965) absorption at z < 6 indicates that the IGM is highly ionized by that epoch (e.g. Fan et al. 2000, 2001, Becker et al. 2001, Djorgovski et al. 2001, Songaila & Cowie 2002). Spectroscopic observations of the highest-redshift quasars and galaxies provide a number of observational constraints suggesting that $z \sim 6$ indeed marks the end of the reionization epoch:

• The detection of complete GP absorption troughs in the spectra of quasars at z > 6 suggests that the neutral fraction of the IGM is increasing rapidly with redshift (Cen & McDonald 2002, Fan et al. 2002, Lidz et al. 2002, White et al. 2003, Gnedin 2004). This feature is consistent with the phase of IGM evolution at which individual HII regions overlapped; at this point, the IGM ionization state evolved rapidly, similar to a phase transition (cf. Songaila 2004 and discussion below). The lower limit of the volume averaged neutral fraction

is $\sim 10^{-3}$ based on Gunn-Peterson measurements, although it could be much higher in the deepest troughs.

- The sizes of large, highly ionized regions around luminous quasars at z > 6 are consistent with those predicted for a quasar "Strömgren sphere" expanding into a surrounding largely neutral IGM (Mesinger & Haiman 2004, Mesinger et al. 2004, Wyithe & Loeb 2004a). The neutral fraction of the IGM is estimated to be as high as > 20% along some lines of sight, considerably higher than the lower limit using the Gunn-Peterson optical depth. But these measurements are made uncertain because of our lack of knowledge of quasar lifetimes, bolometric corrections of quasar luminosities, the bias factor and the clumpiness of the IGM around high redshift quasars (e.g., Yu & Lu 2005, Yu 2005).
- The observed temperature evolution of the IGM at $z \sim 3-5$ suggests that the reionization epoch is not much higher than 8 (Hui & Haiman 2003). In models with reionization at much higher redshift, the IGM cools to a much lower temperature than that observed at $z \sim 2-4$.

Quasars and AGNs are unlikely to provide enough UV photons to reionize the universe at z > 6 (e.g. Fan et al. 2001, Dijkstra et al. 2004, Meiksin 2005). Star forming galaxies at early epochs are the most likely candidates to ionize the IGM, although current observations still have poor constraints on the total ionizing photon budget at $z \sim 6$ (Yan & Windhorst 2004b, Stiavelli et al. 2004). Recent measurements of the luminosity density of Lyman break galaxies using deep HST observations show a moderate decline in total UV luminosity of star forming galaxies at z > 6 (Bunker et al. 2004, Yan & Windhorst 2004b, Bouwens et al. 2004a,b). If the reionization process was similar to a phase transition, the high-redshift quasar observations suggest that the Universe could have been mostly neutral as late as z = 6 - 8.

Polarization measurements of the cosmic microwave background (CMB) based on WMAP first-year data (Kogut et al. 2003) show a large optical depth due to Thompson scattering of electrons ($\tau = 0.17 \pm 0.04$) in the early Universe, suggesting that the IGM was largely ionized by $z \sim 17 \pm 4$. WMAP three-year data (Spergel et al. 2006) show a smaller optical depth ($\tau = 0.09 \pm 0.03$) based on the new EE measurements, indicating a larely ionized IGM by $z \sim 10 \pm 3$. The WMAP polarization results, combined with low redshift constraints, suggest that reionization could be an extended process rather than a phase transition (Cen 2003a, b, Wyithe & Loeb 2003a, Haiman & Holder 2003, Somerville et al. 2003, Gnedin 2004, Choudhury & Ferrara 2005). Even at $z \sim 6$, several lines of evidence suggest that a uniform end of reionization with a clean phase transition in the ionization state is too simplistic:

• While the optical depth no doubt has increased at z > 6, it is not agreed whether the increase is similar to a sharp phase transition (e.g., Fan et al. 2002), or is simply a continuation of the gradual thickening of the Ly α forest (e.g. Songaila 2004). Although optical depth measurements of quasar spectra are consistent among different studies, the different interpretations arise because: (1) complete Gunn-Peterson troughs give only a

lower limit to the optical depth; (2) there are complications in the interpretation of the Ly β measurements; and (3) there is a lack of a clear definition of "gradual" vs. "sharp" transitions.

- There are large line of sight variations from one quasar to another. The GP trough detected in the spectrum of SDSS J1030+0524 (z=6.28, Fan et al. 2001, Becker et al. 2001, White et al. 2003) shows complete absorption in the Ly α , β and γ transitions. However, the line of sight of SDSS J1148+5251 (z=6.42, Fan et al. 2002) shows clear transmission, especially in the Ly β and γ transitions (White et al. 2003, 2005, Oh & Furlanetto 2005), indicating that the IGM along this line of sight is still more than 99% ionized.
- The lack of evolution in the luminosity functions of Ly α emitting galaxies from $z \sim 5.7$ to $z \sim 6.5$ is also consistent with the picture that the IGM is largely ionized at $z \sim 6$; in a largely neutral IGM, an extended Gunn-Peterson absorption damping wing would attenuate the Ly α emission of high-redshift galaxies (Hu et al. 2004, 2005, Malhotra & Rhoads 2004, Stern et al. 2005, Malhotra & Rhoads 2006). However, due to uncertainties in the clustering of Ly α galaxies and the clumpiness of the IGM, a relatively high neutral fraction cannot yet be ruled out by the Ly α emitter observations (Santos 2004, Haiman & Cen 2005, Wyithe et al. 2005, Furlanetto et al. 2006).

Reionization is a complex process which results from the interplay of structure formation, early star formation and feedback, and radiative transfer in a clumpy IGM. Recent developments in both semi-analytic models and simulations aim at understanding these processes in the context of improved observational constraints and future observations. Models that include feedback from the formation of the earliest, metal-free populations can generally fit both the Gunn-Peterson measurements at low redshift and a high CMB polarization measurement (e.g., Cen 2003a, b, Wyithe & Loeb 2003a, Haiman & Holder 2003, Melchiorri et al. 2005). Cosmological simulations with improved resolution, box size and treatment of radiative transfer (e.g. Gnedin 2000, 2004, Razoumov et al. 2002, Paschos & Norman 2005) are beginning to make realistic comparison with observations possible.

To make further progress observationally, spectroscopy of a large sample of luminous sources is needed to explore the line of sight variation in the GP optical depth measurements expected due to clumpiness in the IGM and clustering of ionizing sources (e.g. Wyithe & Loeb 2004b, Paschos & Norman 2005). Fan et al. (2002, Paper I) presented measurements of the ionization state of the IGM at $z \sim 6$ and constraints on the epoch of reionization, using a sample of four quasars at z = 5.74 - 6.28. In this follow-up paper, we describe measurements of Lyman absorption using spectroscopic observations of a sample of nineteen quasars at z = 5.74 - 6.42, discovered from the imaging data of the Sloan Digital Sky Survey (Fan et al. 2000, 2001, 2002, 2003, 2004, 2006). We address the following three questions:

1. How fast do the average and the dispersion of the IGM ionization state evolve in the

redshift range z = 5 - 6.4? In particular, is there a well-defined break in these quantities as a function of redshift?

- 2. Is the IGM consistent with a large neutral fraction at least along some lines of sight? What is the *upper* limit of the neutral fraction when considering all the observational constraints?
- 3. Can we define a set of statistics from the observed spectrum that are also easily extractable from cosmological simulations and allow direct comparison with theoretical models (e.g., Songaila & Cowie 2002, Paschos & Norman 2005)?

The paper is organized as follows: in §2, we describe our spectroscopic sample of 19 SDSS quasars at z=5.74-6.42. In §3, we measure the evolution of Gunn-Peterson optical depths. We present Ly α measurements in §3.1, discuss in detail the optimal way of combining Ly α , β and γ measurements in §3.2, and present the measurement of the dispersion of optical depth along different lines of sight in §3.3. In §4, we derive a number of quantities characterizing the ionization state of the IGM: the evolution of the ionizing background based on a photoionization model (§4.1), and of the mean free path of ionizing photons and the neutral fraction of the IGM (§4.2), following the methods developed in Paper I. We compare these results with simulations in §4.3. In §5, we study the presence of complete Gunn-Peterson absorption troughs in quasar spectra (§5.1), and discuss in detail the statistics of the dark gap distribution (§5.2). In §5.3, we use these statistics to place an independent upper limit on the IGM neutral fraction. In §6, we measure the sizes of HII regions around these 19 quasars, and use their evolution to place an independent constraint on the rate of neutral fraction evolution at $z \sim 6$. Finally, we summarize the results in §7. Through the paper, we use the WMAP cosmology (H₀ = 71 km s⁻¹ Mpc⁻¹, Ω_{Λ} = 0.73, Ω_{M} = 0.27, and Ω_{b} = 0.04, Spergel et al. 2003) to present our results.

2. A Spectroscopic Sample of $z \sim 6$ Quasars

The Sloan Digital Sky Survey (York et al. 2000) is using a dedicated 2.5m telescope (Gunn et al. 2006) and a large format CCD camera (Gunn et al. 1998) at the Apache Point Observatory in New Mexico to obtain images in five broad bands $(u, g, r, i \text{ and } z, \text{ centered at } 3551, 4686, 6166, 7480 \text{ and } 8932 \text{ Å}, \text{ respectively; Fukugita et al. 1996}) of high Galactic latitude sky in the Northern Galactic Cap. About 7500 <math>\deg^2$ of sky in the Northern Galactic Cap have been imaged at the time of this writing (Oct 2005). The imaging data are processed by the astrometric pipeline (Pier et al. 2003) and the photometric pipeline (Lupton et al. 2001), and are photometrically calibrated to a standard star network (Smith et al. 2002; see also Hogg et al. 2001, Ivezic et al. 2004, Tucker et al. 2005).

Quasars with redshift greater than 5.7 are characterized by very red i-z colors. Since 2000, we have been using the imaging data from the SDSS to select *i*-dropout candidates. At z > 5.7, all quasars have deep Ly α absorption and satisfy our color-selection criteria (i-z > 2.2); the



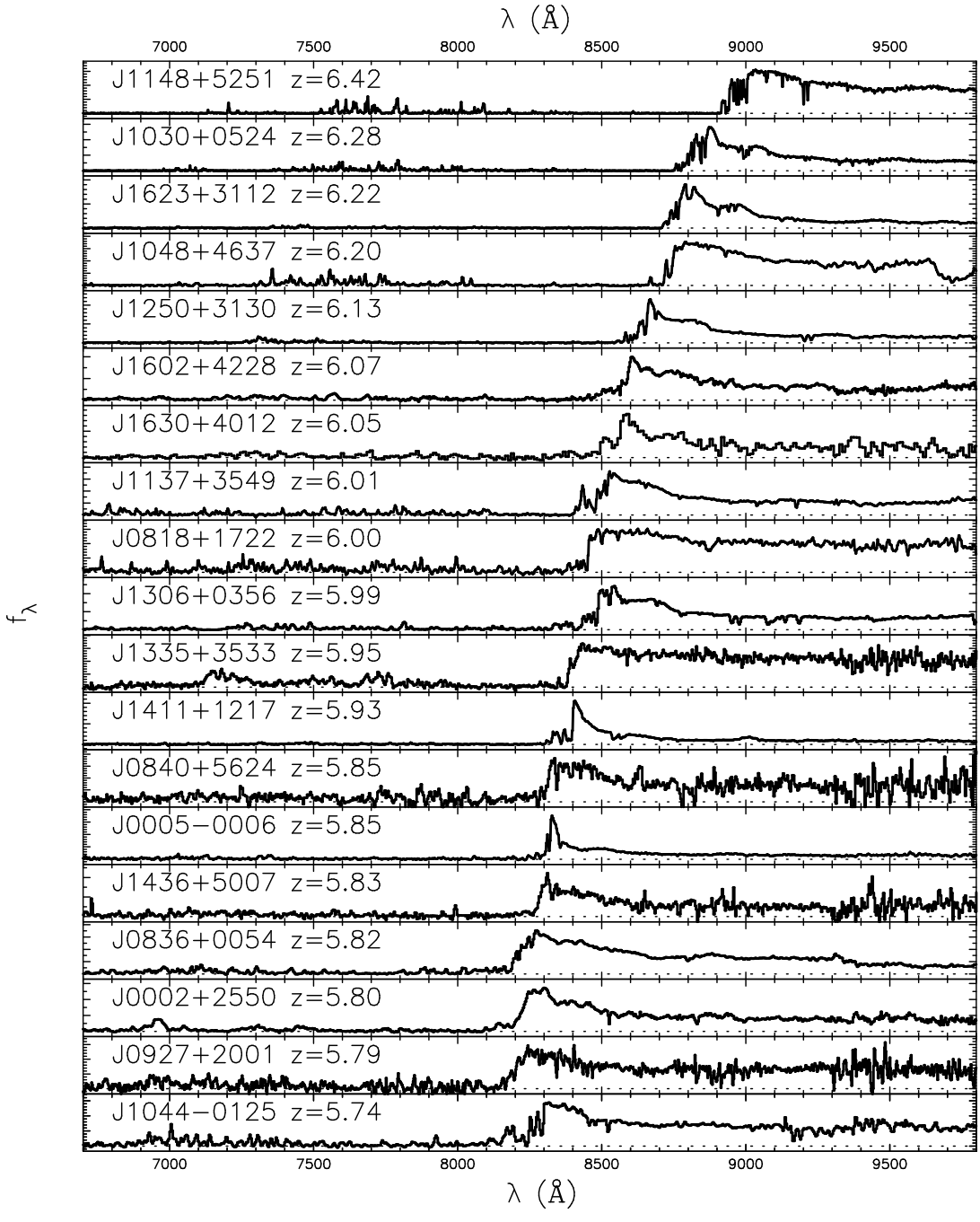


Fig. 1.— Spectra of our sample of nineteen SDSS quasars at 5.74 < z < 6.42. Twelve of the spectra were taken with Keck/ESI, while the others were observed with the MMT/Red Channel and Kitt Peak 4-meter/MARS spectrographs. See Table 1 for detailed information.

color-selection will not bias IGM measurements. Because such quasars are very red and faint, and can be confused with cosmic rays and brown dwarfs, we do not use the automated SDSS quasar selection algorithm (Richards et al. 2002a) to select and target them. In a series of papers (Fan et al. 2000, 2001, 2003, 2004, 2006), we have reported the selection and identification of nineteen quasars selected from about 6600 deg² of SDSS imaging. The sample covers the redshift range z = 5.74 - 6.42, and a range of absolute magnitudes in rest-frame 1450Å, $M_{1450} = -26.2$ to -27.9. They are the most distant luminous quasars published to date (see also Mahabal et al. 2005, R. Cool et al. in preparation).

Table 1 summarizes the properties and spectroscopic observations of these quasars. These spectra were taken with a number of different spectrographs and exposure times, resulting in a range of signal-to-noise ratio (S/N) and spectral resolution. Twelve objects in the sample have spectra taken with the Echellette Imaging Spectrograph (ESI, Epps & Miller 1998) on the Keck II telescope, of which four are presented in this paper for the first time (see White et al. 2003 for details of observations and data reduction). These data have spectral resolution $R \sim 3000-6000$. depending on the seeing and slit used. To present uniform data, we have binned all the Keck/ESI spectra to a resolution of R=2600. Although the S/N of these spectra vary by a factor of ~ 7 , we have sufficiently long observations for all quasars at z > 6.1 to ensure proper measurement of complete Gunn-Peterson troughs. For quasars at z < 6.1, and absorption redshift $z_{abs} < 5.7$, the IGM transmission is well detected even with relatively short exposures. In most of this paper, we will use averaged transmission and effective optical depth as the main observables. The non-uniform S/N among the lower redshift quasars is not a limiting factor in the analysis: in fact, uncertainties in the average transmission are dominated by large sample variance (§3.3). Thus our data are adequate for our purposes, although calculating higher-order statistics requires more uniformly high S/N spectra, such as presented by White et al. (2003), Songaila (2004) and Becker et al. (2006).

3. Evolution of Gunn-Peterson Optical Depth

Figure 1 presents the spectra of the 19 quasars. At least two of the objects (SDSS J1048+4637 12 , z=6.20, Maiolino et al. 2004, and SDSS J1044-0125, z=5.74, Djorgovski et al. 2001, Goodrich et al. 2001) are broad absorption line (BAL) quasars. In analyzing their spectra, we have excluded regions that are affected by the Ly α and Ly β BAL features. Our optical spectroscopy is usually adequate to detect SiIV BAL troughs. However, at $z\sim6$, the strongest CIV BAL troughs are redshifted to $\lambda\gtrsim1\mu\mathrm{m}$. Fewer than half of the objects in the sample have adequate IR spectroscopic observations to detect the CIV BAL feature. Note that the fraction of BAL quasars at z<4 is $\sim15\%$ in color-selected samples (e.g. Reichard et al. 2003).

¹²Throughout this paper, we use the shortened version of quasar name, SDSS Jhhmm+ddmm. Complete IAU names are given in Table 1.

Figure 1 shows strong redshift evolution of the transmission of the IGM: transmitted flux is clearly detected in the spectra of quasars at z < 6 and blueward of the Ly α emission line; the absorption troughs deepen for the high-redshift quasars, and complete Gunn-Peterson absorption begins to appear along lines of sight at z > 6.1. In this section, we present detailed measurements of the average Gunn-Peterson optical depth in the Ly α , β and γ transitions and discuss the variation of the optical depth along different lines of sight.

3.1. Ly α

The Gunn-Peterson (1965) optical depth to Ly α photons is

$$\tau_{\rm GP} = \frac{\pi e^2}{m_e c} f_\alpha \lambda_\alpha H^{-1}(z) n_{\rm HI},\tag{1}$$

where f_{α} is the oscillator strength of the Ly α transition, $\lambda_{\alpha} = 1216\text{Å}$, H(z) is the Hubble constant at redshift z, and $n_{\rm HI}$ is the density of neutral hydrogen in the IGM. At high redshifts, using $H(z) \propto h\Omega_m^{1/2}(1+z)^{3/2}$, and converting hydrogen density to the present-day baryon density parameter Ω_b , the GP optical depth for a uniformly distributed IGM can be re-written as:

$$\tau_{\rm GP}(z) = 1.8 \times 10^5 h^{-1} \Omega_m^{-1/2} \left(\frac{\Omega_b h^2}{0.02} \right) \left(\frac{1+z}{7} \right)^{3/2} \left(\frac{n_{\rm HI}}{\langle n_{\rm H} \rangle} \right).$$
(2)

We define the transmitted flux ratio as the average ratio of observed flux to that in the absence of absorption:

$$T(z_{\rm abs}) \equiv \left\langle f_{\nu}^{\rm obs} / f_{\nu}^{\rm int} \right\rangle,$$
 (3)

where the average is over a certain wavelength or redshift range along the line of sight. We also define the effective GP optical depth,

$$\tau_{\rm GP}^{\rm eff} \equiv -\ln(\mathcal{T}).$$
(4)

Note that for a clumpy IGM, most of the flux is transmitted through regions with low $n_{\rm HI}$, while high density regions simply saturate, resulting in a much smaller effective optical depth than the average of the pixel-to-pixel optical depth, $\tau^{\rm eff} < \langle \tau \rangle$ (for further discussion, see Paper I, Oh & Furlanetto 2005, and §4 of this paper).

We measure the transmitted flux ratio in the Ly α transition as a function of redshift for the sample of 19 quasars as follows: (1) we define the maximum redshift z_{max}^{α} as the maximum Ly α absorption redshift which is not affected the proximity effect from the quasar itself (§6). For the two known BAL quasars, regions affected by the BAL are excluded based on their SiIV and CIV absorption redshifts. For non-BAL quasars, we find $z_{\text{em}} - z_{\text{max}}^{\alpha} = 0.07 - 0.23$, with the difference increasing towards lower redshift and higher luminosity (§6). (2) The minimum absorption redshift considered is chosen as $1 + z_{\text{min}}^{\alpha} = (1 + z_{\text{em}}) \times 1040 \text{Å}/\lambda_{\alpha}$, where 1040 Å is the shortest wavelength

that is not affected by the Ly β +OVI emission line. The redshift interval covered by each line of sight ranges from 0.76 to 0.98. (3) We choose a redshift interval $\Delta z = 0.15$ for the calculation of the average in Eq. (3). This interval corresponds to ~ 60 Mpc in co-moving distance at $z \sim 6$, larger than any large-scale structure at that redshift (see §4.1). It is also sufficiently wide that the measurement error due to photon noise is always small in the absence of complete GP troughs. (4) We assume an underlying intrinsic spectrum with a power law continuum $f_{\nu} \propto \nu^{-0.5}$ (Vanden Berk et al. 2001) and a double Gaussian Ly α +NV emission line. The transmitted flux is measured by extrapolating this intrinsic spectrum $f_{\nu}^{\rm int}$ to shorter wavelength. When $\mathcal T$ approaches zero at high redshift, the optical depth measurement depends only logarithmically on the exact shape of the power law continuum. As discussed in detail in Paper I, the dominant error of the optical depth measurement is sample variance in different regions of the IGM. The Ly α +NV emission line is only important for the region closest to the Ly α emission line in the quasar proximity zone (§6). For the whole sample, the Ly α transmitted flux measurements cover a redshift range of $4.9 < z_{\rm abs} < 6.3$, with a total length of 14.6 in redshift (~ 6000 comoving Mpc) when adding up all lines of sight.

Table 2 presents the measurements of the Ly α transmitted flux ratio. Figure 2 presents the effective optical depth for the Ly α transition as a function of redshift. When flux is detected at less than the 2- σ level, a 2- σ lower limit on the optical depth is used. At $z_{\rm abs} < 4.9$, we plot the data from Songaila (2004), where 95% variation due to sample variance is shown for each redshift. The dashed curve shows the best-fit power-law for $z_{\rm abs} < 5.5$:

$$\tau_{\rm GP}^{\rm eff} = 0.85 \times \left(\frac{1+z}{5}\right)^{4.3}.$$
(5)

The results here are consistent with those in previous papers, now using a significantly larger sample at $z_{\rm abs} > 5.7$. While at $z_{\rm abs} < 5.7$, the evolution of optical depth closely follows the $(1+z)^{4.3}$ power law, there appears to be an accelerated evolution at $z_{\rm abs} \gtrsim 5.7$, where the optical depth rapidly exceeds a simple extrapolation from lower redshift.

In addition to the increase in the average Ly α optical depth, there is also an increase in the dispersion of this measurement. Dark regions with $\tau_{\rm GP}^{\rm eff} > 5.5$ occur as early as $z_{\rm abs} \sim 5.7$. Deep, complete GP absorption troughs are detected in three different lines of sight with various redshifts and lengths (§4.2). For example, at $z_{\rm abs} > 5.9$, we have eight independent measurements, resulting in two upper limits ($\tau_{\rm GP}^{\rm eff} > 6 - 7$) and six detections ($\tau_{\rm GP}^{\rm eff} = 3.9 - 6.5$). The smallest optical depth measured at z > 6 does not deviate significantly from the low-redshift extrapolation (see e.g. Songaila 2004). We discuss the increasing dispersion of optical depth in §3.3.

3.2. Ly β and Ly γ

At a given absorption redshift, the GP optical depth $\tau_{\rm GP} \propto f \lambda$, where f and λ are the oscillator strength and rest-frame wavelength of the transition. For the same neutral hydrogen

.

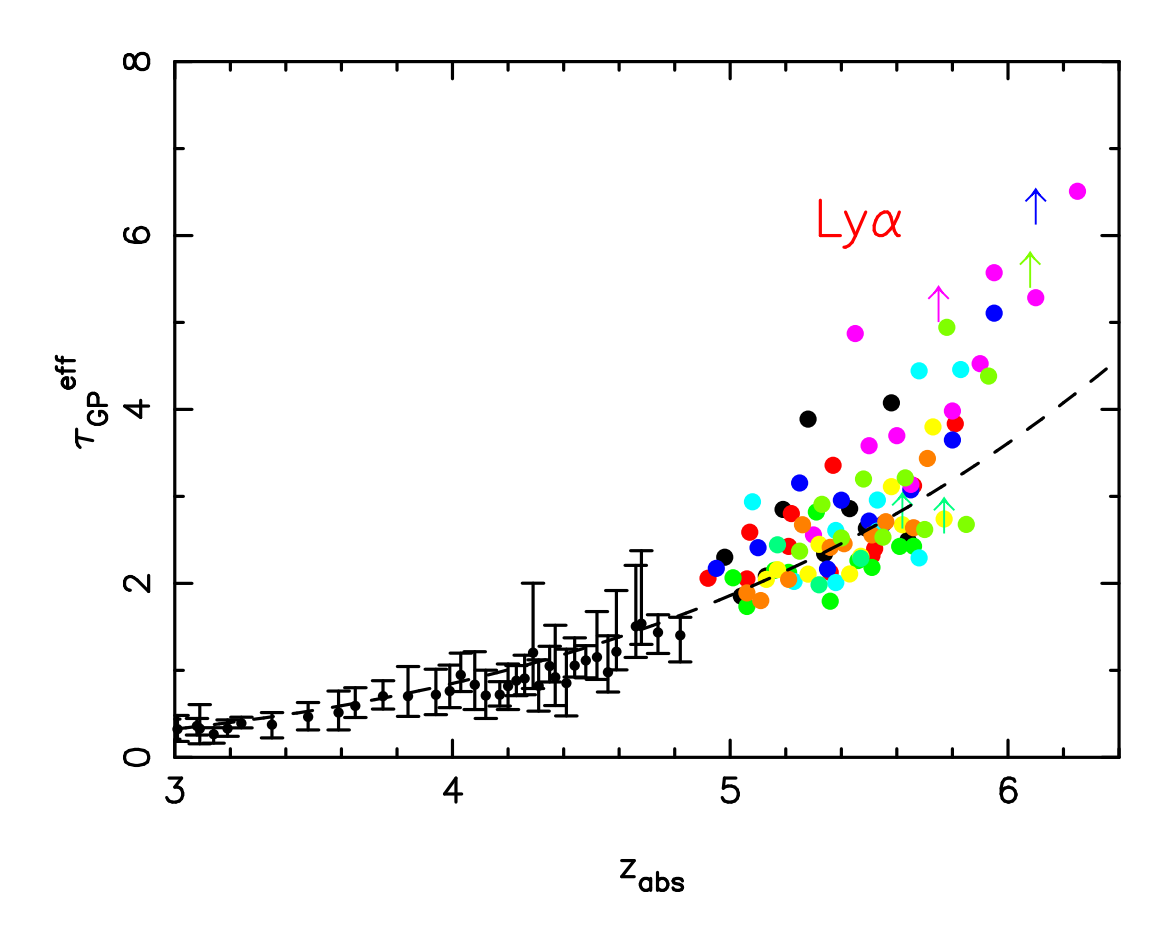


Fig. 2.— Evolution of the Ly α Gunn-Peterson optical depth with redshift averaged over intervals $\Delta z = 0.15$ along each line of sight. At $z_{\rm abs} = 4.8-6.3$, the sample of 19 quasars in this paper yields a total of 97 independent measurements covering a total redshift interval of $\Delta z = 14.6$ (large symbols). In complete GP troughs in which no flux is detected, the 2- σ lower limit on optical depth is indicated with an arrow. We also include the measurements at lower redshift from Songaila (2004, small symbols). The dashed curve shows the best-fit power-law for $z_{abs} < 5.5$: $\tau_{\rm GP}^{\rm eff} = (0.85 \pm 0.06) \times \left(\frac{1+z}{5}\right)^{4.3 \pm 0.3}$. At $z_{\rm abs} \gtrsim 5.7$, the evolution accelerates, with increased dispersion and a rapid deviation from the power-law relation.

density, the GP optical depths of Ly β and Ly γ are factors of 6.2 and 17.9 smaller than that of Ly α , respectively. When Ly α absorption saturates at z > 6, Ly β and Ly γ can in principle provide more stringent constraints on the IGM ionization state. However, just as we have seen that the average and effective GP optical depths are different, in a clumpy IGM, the ratio of effective optical depths between Ly α and Ly β / Ly γ transition are smaller than the factors above. The Ly β /Ly γ absorptions in the quasar spectra are further affected by the lower order transitions in the foreground (at lower $z_{\rm abs}$) which have to be removed when measuring optical depth. In this subsection, we first present direct measurements of Ly β absorption, then discuss the ratio of optical depths among different transitions. Ly γ measurements are discussed at the end of this subsection.

We measure the Ly β transmission using the same procedure as for Ly α . The minimum redshifts for the Ly β measurements are chosen as: $1+z_{\min}^{\beta}=(1+z_{\min})\times 970\text{Å}/\lambda_{\beta}$ to avoid contamination from Ly γ absorption. Because of this, 15 of the 19 lines of sight have only one independent measurement at $\Delta z=0.15$. Two lines of sight have two independent data points, while two others have an uncontaminated Ly β redshift interval narrower than 0.15. The Ly β measurements cover a redshift range of $5.3 < z_{\rm abs} < 6.3$ with a total redshift interval of 2.9. Table 3 presents the observed transmitted flux ratio in the Ly β region, without correcting for the foreground Ly α absorption. Figure 3 presents the GP optical depth due to Ly β absorption along the nineteen lines of sight in our sample, as well as lower redshift measurements from Songaila (2004). In Figure 3, we have corrected for the foreground Ly α absorption at $z'_{\rm abs}=(1+z_{\rm abs})\lambda_{\beta}/\lambda_{\alpha}-1$, using Eq. (5) above. Note that while this correction is statistically correct, it increases the dispersion of the Ly β GP optical depth. The dashed line in Figure 3 is the best-fit relation at $z_{abs}<5.5$:

$$\tau_{\beta}^{\text{eff}} = (0.38 \pm 0.05) \times \left(\frac{1+z}{5}\right)^{4.3 \pm 0.3}$$
 (6)

We fixed the power-law index to be the same as Eq. (5) in the fit. Compared to Figure 2, the deviation from the power-law relation at $z_{abs} > 5.7$ is more pronounced in term of the ratio of optical depths: at $z_{abs} \sim 6$, the lower limit on the average Ly β optical depth is ~ 3.5 , compared to the extrapolated value of 1.7 from Eq. (6). Also note that among the three Ly α lower limits in Figure 2 that also have valid Ly β measurements, one has a clear detection of flux in Ly β , indicating that Ly β is indeed more sensitive to large neutral fraction than Ly α . The two other Ly β points, however, still do not have detectable flux, suggesting a high neutral fraction.

A number of authors have studied the evolution of the ionizing background and neutral fraction of the IGM by combining Ly α and Ly β measurements (Paper I, Cen & McDonald 2002, Lidz et al. 2002). They show that the Ly β measurements indeed yield stronger constraints on the ionizing background at $z_{\rm abs} > 6$. Songaila (2004) and Oh & Furlanetto (2005) explicitly estimated the ratio of effective optical depths in the two transitions in a clumpy IGM. Here we expand the discussion in Paper I, and calculate the ratios using two independent methods. Note that in Paper I, the difference between the Ly α and Ly β wavelengths was neglected in the calculations, resulting

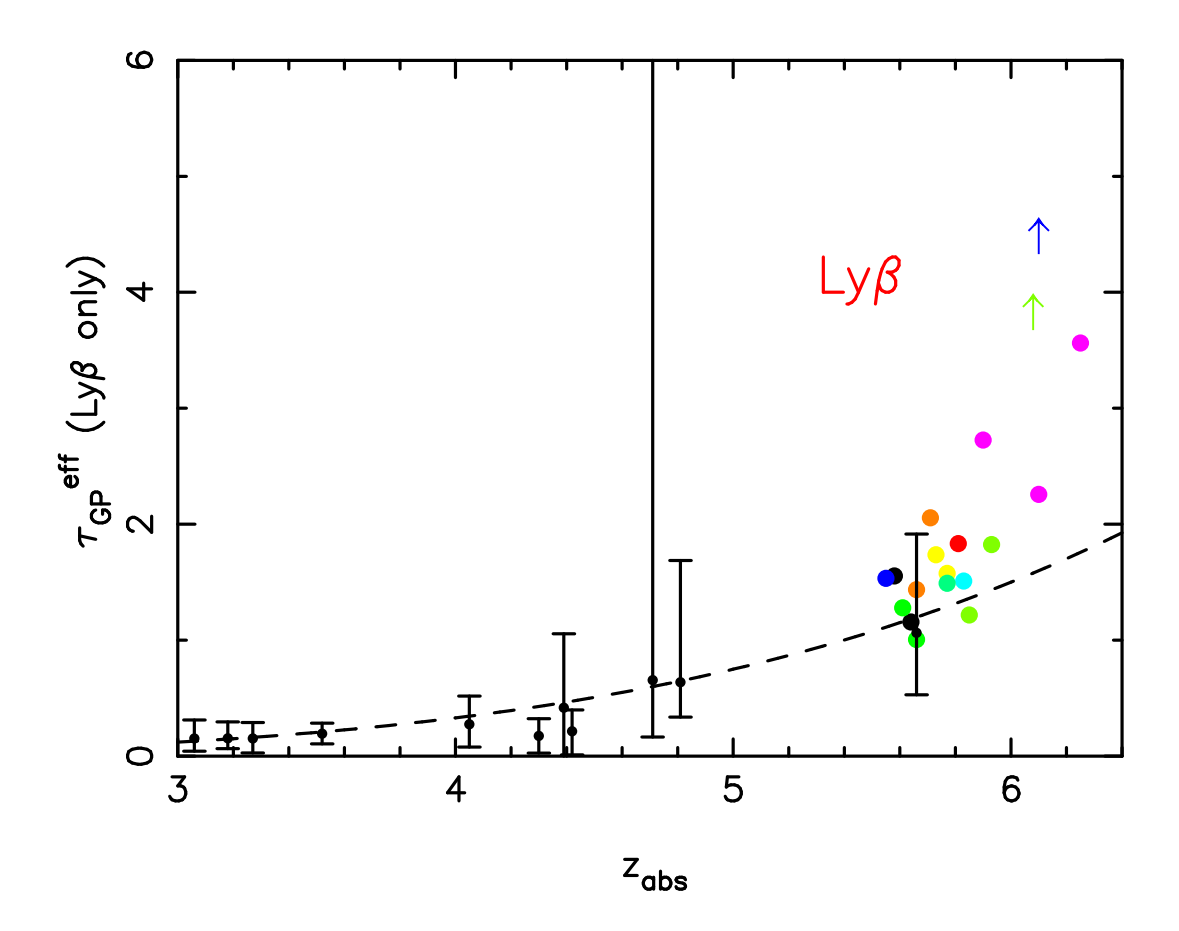


Fig. 3.— Evolution of the Ly β Gunn-Peterson optical depth with redshift. At $z_{\rm abs}=5.3-6.3$, there are 19 independent measurements covering a total redshift interval of $\Delta z=2.9$. These measurements have been corrected for the foreground Ly α absorption. We also plot the measurements at lower redshift from Songaila (2004). The dashed curve shows the best-fit power-law for $z_{abs}<5.5$: $\tau_{\beta}^{\rm eff}=0.38\times\left(\frac{1+z}{5}\right)^{4.3}$. Like Ly α , at $z_{\rm abs}\gtrsim5.7$, the evolution accelerates with a rapid deviation from the power-law relation.

in an estimated ionizing background that was 7% too high at $z_{abs} > 6$ (see §4.1).

We first estimate the conversion factor using a model in which the IGM is isothermal and photo-ionized by an uniform UV background, following Paper I and similar treatments by other authors. A detailed discussion of the formalism can be found in Paper I, and will only be described briefly here. We define the fractional density of the IGM as $\Delta \equiv \rho/\langle \rho \rangle$. Assuming local photoionization equilibrium, whereby the netural hydrogen fraction depends on the square of the local density, one can show that for a region of IGM with density Δ ,

$$\tau(\Delta) \propto \frac{(1+z)^{4.5} (\Omega_b h^2)^2 \alpha [T(\Delta)]}{h \Gamma(\Delta, z) \Omega_m^{0.5}} \Delta^2, \tag{7}$$

where Γ is the photoionization rate, assumed to be uniform here, and $\alpha(T)$ is the recombination coefficient at temperature T (Abel et al. 1997), $\alpha(T) = 4.2 \times 10^{-13} (T/10^4 \text{K})^{-0.7} \text{cm}^3 \text{s}^{-1}$. The relation $T(\Delta) \propto \Delta^{\gamma}$ is the equation of state of the IGM, where $\gamma = 0 - 1$. We assume $\gamma = 0$ for isothermal case here. The observed transmitted flux ratio or effective optical depth is averaged over the entire IGM density distribution,

$$\mathcal{T} = \langle e^{-\tau} \rangle = \int_0^\infty e^{-\tau(\Delta)} p(\Delta) d(\Delta), \tag{8}$$

where $p(\Delta)$ is the distribution function of the density of the IGM. We calculate \mathcal{T} in a clumpy IGM using a parametric form for the volume-weighted density distribution function $p(\Delta)$ (Miralda-Escudé, Haehnelt, & Rees 2000):

$$p(\Delta) = A \exp\left[-\frac{(\Delta^{-2/3} - C_0)^2}{2(2\delta_0/3)^2}\right] \Delta^{-\beta},\tag{9}$$

where $\delta_0 = 7.61/(1+z)$, and β , C_0 and A are numerical constants given in Table 1 of Miralda-Escudé et al. (2000) at several redshifts, derived from their simulation which assumed a cosmology consistent with that of WMAP. We linearly interpolate these constants as a function of redshift. Eq. (7) is appropriate for all Lyman series lines, with different values of the proportionality constant. Eq. (7) also shows that if the ionizing background and the clumpiness of the IGM do not evolve with redshift, then $\tau \propto (1+z)^{4.5}$. At $z_{\rm abs} < 5.5$, this is the leading term in the observed scaling relation (Eqs. 5 and 6), and the increasing clumpiness and decreasing ionizing background as one moves to lower redshift roughly cancel each other out. A significant deviation from this relation (§3.3) indicates an accelerated evolution in the ionizing background.

We calculate the GP optical depth in different Lyman transitions as a function of IGM photoionization rate at z=6. Figure 4 shows the conversion factors $\tau_{\alpha}^{\text{eff}}/\tau_{\beta}^{\text{eff}}$ and $\tau_{\alpha}^{\text{eff}}/\tau_{\gamma}^{\text{eff}}$ as a function of the photoionization rate Γ_{-12} , in units of 10^{-12} s^{-1} . The conversion factor shows a mild dependence on the ionizing background. For parameters of interest (see §4.1), $\Gamma_{-12}=0.01-0.25$, the Ly α - Ly β conversion factor $\tau_{\alpha}^{\text{eff}}/\tau_{\beta}^{\text{eff}}=2.5-2.9$, and the Ly α - Ly γ conversion factor $\tau_{\alpha}^{\text{eff}}/\tau_{\gamma}^{\text{eff}}=4.4-5.7$. These values are factors of 2-4 smaller than those in the case of a uniform IGM, consistent with those found by Oh & Furlanetto (2005).

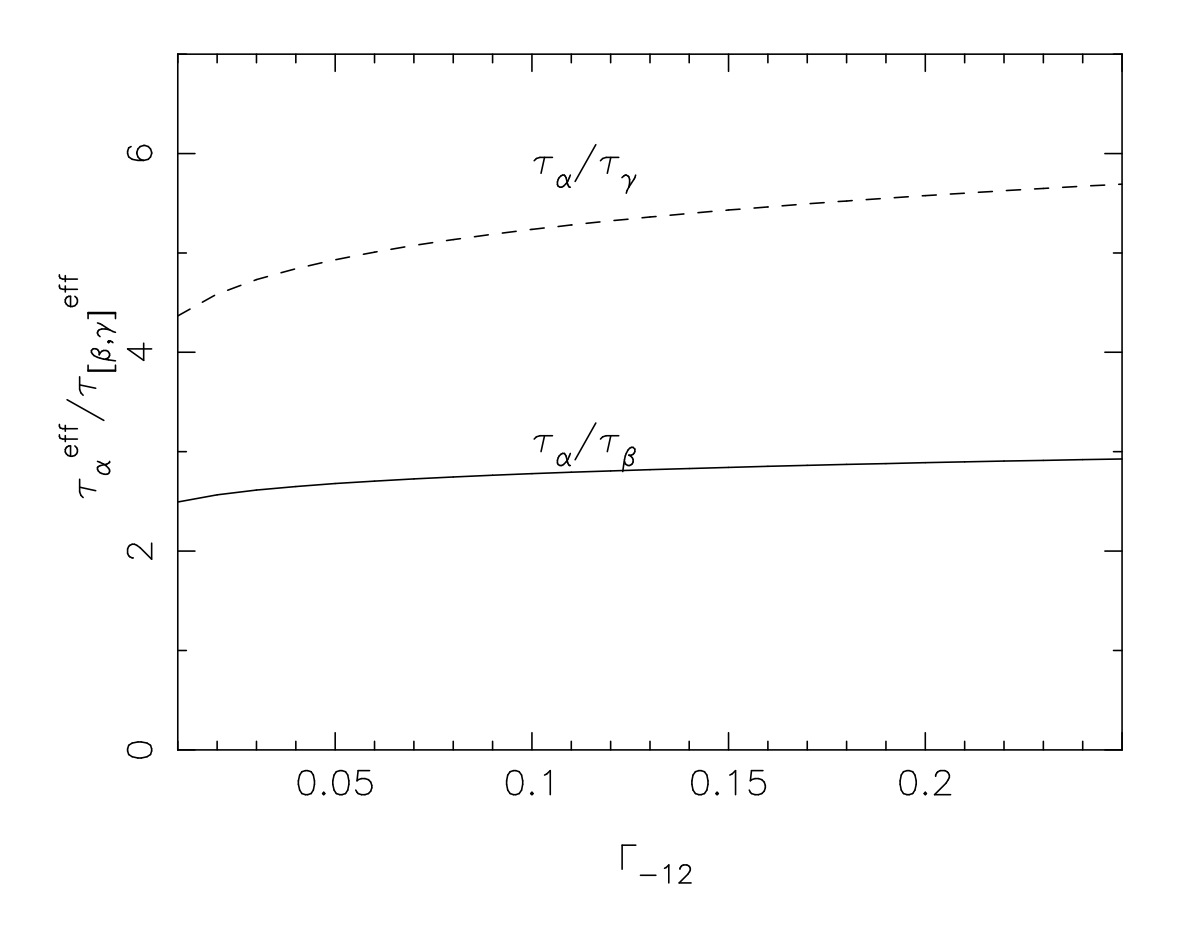


Fig. 4.— The optical depth conversion factors between Lyman series transitions as a function of the UV background at z=6. For a clumpy, isothermal IGM and a uniform background, the Ly α - Ly β conversion factor lies in the range of 2.5 – 2.9, while the Ly α - Ly γ conversion factor lies between 4.4 and 5.7.

The calculation above is subject to the assumptions we made about the clumpiness of the IGM, its equation of state, and the uniformity of the ionizing background. We also calibrate the Ly α - Ly β conversion factor empirically: we calculate the average transmitted flux ratios (not the average optical depth) in Ly α and Ly β over the same redshift range, \mathcal{T}_{α} and \mathcal{T}_{β} , the latter corrected for foreground Ly α absorption, and define the conversion factor as: $\tau_{\alpha}^{\text{eff}}/\tau_{\beta}^{\text{eff}} = \ln(\mathcal{T}_{\beta}/\mathcal{T}_{\alpha})$. This method simply requires that the Ly α and Ly β measurements yield consistent results on the optical depth and neutral fraction. We find that for $z_{abs} = 5.4 - 5.8$: $\tau_{\alpha}^{\text{eff}}/\tau_{\beta}^{\text{eff}} = 2.25$, and for $z_{abs} > 5.9$, $\tau_{\alpha}^{\text{eff}}/\tau_{\beta}^{\text{eff}} = 2.19$. This conversion factor is somewhat smaller than that found using the photo-ionization model. Oh & Furlanetto (2005) show that a more clumpy IGM, or a UV background in which Γ is correlated with density, results in a smaller conversion factor. For the remainder of this paper, we adopt the conversion factors: $\tau_{\alpha}^{\text{eff}}/\tau_{\beta}^{\text{eff}} = 2.25$, and $\tau_{\alpha}^{\text{eff}}/\tau_{\gamma}^{\text{eff}} = 4.4$. We will use the notation $\tau_{\text{GP}}^{\text{eff}}$ as the effective optical depth converted to the Ly α transition unless otherwise noted.

The measurement of Ly γ optical depth is severely restricted by the presence of Ly δ absorption at the low-redshift end and the quasar proximity effect at the high-redshift end. Only the three lines of sight towards the three highest redshift quasars at z>6.2 provide a redshift range $\Delta z>0.06$ for this measurement. As before, the Ly γ optical depth has been corrected for foreground absorption in Ly α and Ly β , using Eqs. (5) and (6) and converted to the Ly α values. The results are summarized in Table 4. In all three cases, the Ly β regions probed correspond to redshift ranges with deep Ly α GP troughs.

3.3. Accelerated Evolution of the Average and Scatter of GP Optical Depth

Figure 5 shows the combined measurements of optical depth evolution using the Ly α , Ly β and Ly γ transitions, with Ly β and Ly γ measurements converted to their Ly α equivalent assuming conversion factors of 2.25 and 4.4, respectively. For $z_{\rm abs}=4.9-6.3$, we have also calculated the mean and standard deviations of $\tau_{\rm GP}^{\rm eff}$ among different lines of sight at a redshift interval of 0.2 based on Ly α and Ly β measurements. When calculating the average and standard deviation, for points where both Ly α and Ly β measurements are available, we use the Ly α measurements in the cases where there is detected Ly α transmitted flux, and use the Ly β measurements or lower limits when no Ly α flux is detected, regardless whether Ly β flux is detected. When there is a non-detection, we simply use the 2- σ lower limit values to calculate the average and standard deviation. Therefore, they are lower limits for the two highest redshift bins. The results are tabulated in Table 5. We do not use Ly γ measurements in Figure 5 to calculate the average and standard deviation, because they only cover a small redshift range. Including Ly γ measurements increases the values of both the average and the scatter of the GP optical depth.

From the figure, we note that:

(1) At z < 6, the Ly α and Ly β measurements are fully consistent. This is a result of the

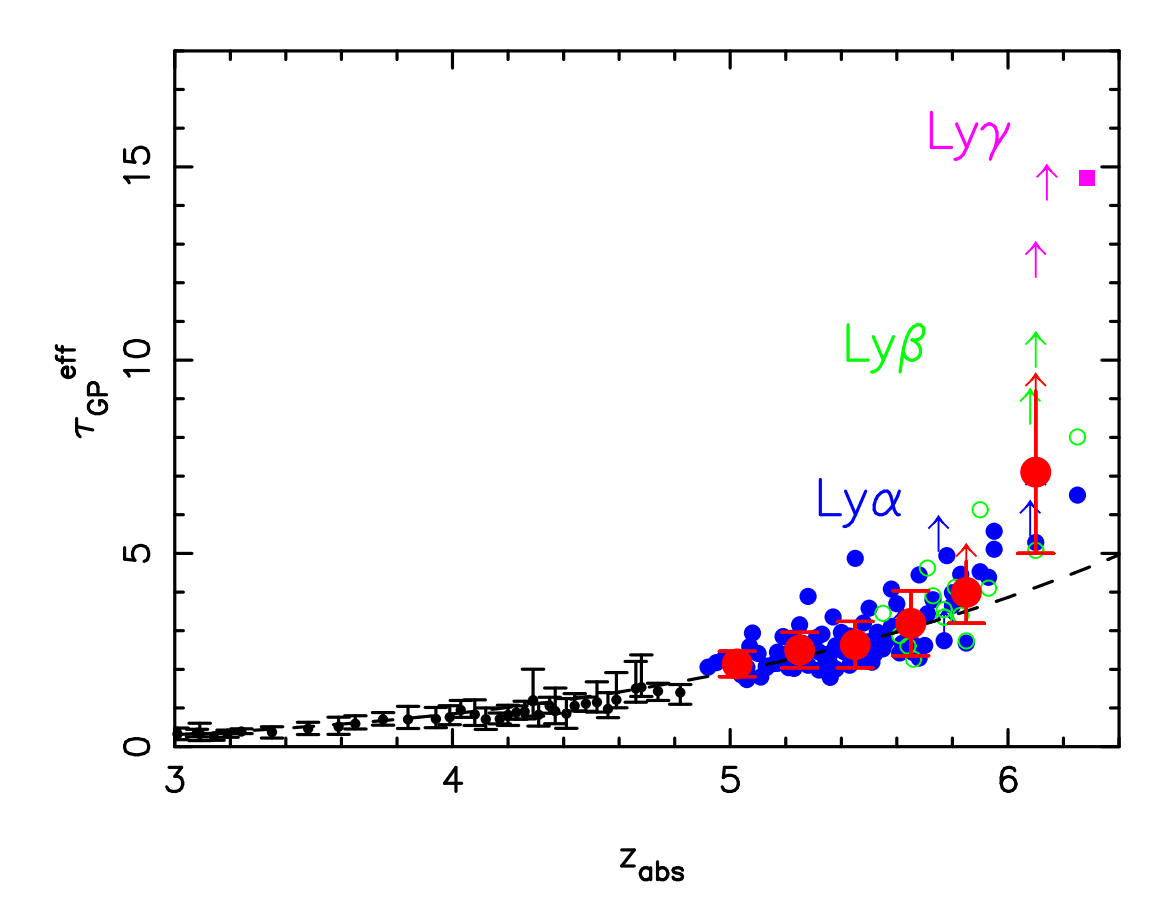


Fig. 5.— Evolution of optical depth with combined the Ly α , Ly β and Ly γ results. The Ly β measurements are converted to Ly α GP optical depth using a conversion factor of 2.25. The values in the two highest redshift bins are lower limits since they both contain complete GP troughs. The dashed line is a redshift evolution of $\tau_{\rm GP}^{eff} \propto (1+z)^{4.3}$. At z>5.5, the best fit evolution has $\tau_{\rm GP}^{eff} \propto (1+z)^{>10.9}$, indicating an accelerated evolution. The large filled symbols with error bars are the average and standard deviation of optical depth at each redshift. The sample variance also increases rapidly with redshift. We also include the Ly γ measurements (square symbol, Table 4); they cover only the high redshift end of the Ly α and Ly β bins due to contamination from Ly δ absorption along the line of sight at lower redshift.

calibration procedure used above. At the highest redshift when no Ly α flux is detected, the Ly β optical depth measurement either gives a secure optical depth measurement that is somewhat higher than the Ly α lower limit (in one case), or provides a much more stringent lower limit (in two cases). Note that the Ly γ measurements only cover the high redshift end of each bin at which the absorption is particularly strong.

(2) With the additional constraints from Ly β measurements, the trend of accelerated evolution in optical depth is clearly established: at $z_{abs} = 5.85$, the lower limit on the averaged optical depths is 4.0, compared to the extrapolated value of 3.3 based on Eq. (5); and at $z_{abs} = 6.1$, the lower limit on the averaged optical depths is 7.1, compared to the extrapolated value of 3.8. We fit a power-law for redshifts $z_{abs} > 5.5$, and find that

$$\tau_{\rm GP}^{\it eff} \propto (1+z)^{>10.9}, \quad z_{\rm abs} = 5.5 - 6.3.$$
 (10)

This should be compared with $\tau_{\rm GP} \propto (1+z)^{4.3}$ at lower redshift, indicating a rapid change in the evolution of optical depth.

(3) The accelerated evolution of the optical depth is accompanied by an increase in the dispersion of the optical depth: at $z_{abs} < 5.0$, the standard deviation $\sigma(\tau) \sim 0.3$. It increases to $\sigma(\tau) \sim 0.6$ at $z_{abs} = 5.5$, and $\sigma(\tau) \sim 0.8$ at $z_{abs} = 5.8$. At $z_{abs} > 6.0$, the lower limit on $\sigma(\tau)$ is 2.1. The increased dispersion $z_{abs} > 5.7$ is due to the fact that some lines of sight have complete GP troughs, with others have optical depths only mildly higher than the power-law extrapolation from low redshift. Different data points are independent measurements of the optical depth in different IGM regions (§4.1). This result suggests that the ionization state of the IGM has large sample variance at the end of reionization (§5).

Using a log-normal density distribution, and carrying out the integral of Eqs. (7), (8), and (9), Songaila & Cowie (2002) found:

$$\tau_{\rm GP}^{\rm eff} = A^{1/(1+3\beta/4)} - \frac{0.83}{\beta + 4/3} \ln(A) + \text{const}, \tag{11}$$

where $A \propto 1/\Gamma$, and $\beta = 2 - 0.7\gamma$ for an uniform radiation background (see also Oh & Furlanetto 2005). If the IGM is isothermal ($\beta = 2$), we have $\tau^{\rm eff} \propto \Gamma^{-0.4}$ as the leading term. This scaling is not sensitive to the detailed IGM density distribution (Eq. 9). Therefore, the evolution of the GP optical depth is driven by the rate of evolution in the UV background: if we observe that the GP optical depth increases by ~ 2.5 from $z \sim 5.5$ to 6.2, we can infer that the UV background decreases roughly by an order of magnitude. We carry out a detailed calculation in the next section.

4. Evolution of the Ionization State of the IGM

In Paper I, we used the evolution of the GP optical depth and the formalism described in Eqs. (7) - (9) to calculate a number of IGM ionization parameters, including the ionizing

background and neutral fraction of the IGM. We also calculated the mean free path of ionizing photons using the model of Miralda-Escudé, Haehnelt, & Rees (2000). Here we carry out similar calculations with the new dataset, and introduce an alternative way of deriving the mean free path. However, we caution that the ionization parameters derived in this section are model dependent: they assume a particular model of the IGM density distribution and photoionization equilibrium with a uniform ionizing background. We will discuss the limitations of these derived properties in detail in subsequent subsections.

4.1. Ionizing Background

Figure 6 shows the estimated photoionization rate evolution with redshift based on Eqs. (7) to (9) and the GP optical depth measurements in Figure 5. Details of these calculations are discussed by McDonald & Miralda-Escudé (2001) and in Paper I. Consistent with the trend seen in Paper I, the drop of ionizing background accelerates at $z_{abs} > 5.7$: from $z_{abs} = 5.6$ to 6.1, Γ declines by a factor of > 4. In the deepest GP troughs, the 2- σ upper limit of the photoionizing rate derived from the Ly β transition is $\Gamma_{-12} < 0.025$. The most stringent constraint comes from the Ly γ measurement (Table 4) in quasar J1030+0524 at $z_{abs} = 6.11 - 6.17$, where $\tau_{GP} > 14.2$ (2- σ) is consistent with a photoionizing rate $\Gamma_{-12} < 0.012$ in that region of the IGM, more than an order of magnitude lower than the average background at $z_{abs} = 5.5$. Also note the relatively flat evolution between $z_{abs} = 5$ and 5.5. This lack of evolution in Γ was first noted by Cen & McDonald (2002) in a small sample of SDSS quasars. The IGM ionizing background is expected to increase towards lower redshift as the emissivity from star forming galaxies and AGNs increases and the photon mean free path increases. Cen & McDonald (2002) suggested that the flattening might be due to the change in the star formation rate as the temperature and Jeans mass rises shortly after reionization.

Just as we saw in Figure 5, there is also a rapid increase in the dispersion of the estimates of the ionizing background. At $z \sim 5$, the relative dispersion $\sigma(\Gamma)/\Gamma$ is $\sim 30\%$. It increases to $\sim 50\%$ at $z \sim 5.5$. At z > 6, $\sigma(\Gamma)/\Gamma > 100\%$ with Γ_{-12} measurements ranging from < 0.02 to ~ 0.09 , reflecting the fact that some lines of sight have complete GP troughs while others still have detectable transmission. In the photoionization model, the observed fluctuation could be due to two effects: (1) large scale fluctuations in the underlying density field due to the finite length of the line of sight used in the measurement, or (2) intrinsic fluctuations in the UV background and/or temperature of the IGM.

Data at $z_{\rm abs} > 4.8$ in Figure 6 are derived from an effective optical depth over $\Delta z = 0.15$ (§4.1), corresponding to $44h^{-1}$ comoving Mpc at $z \sim 6$. The *one-dimensional* rms fluctuation of the average mass density along a line of sight with length L is given by:

$$\sigma_m^2(L) = \frac{1}{2\pi} \int_0^\infty dk \langle \tilde{F}_k^2 \rangle \tilde{W}^2(kR), \tag{12}$$

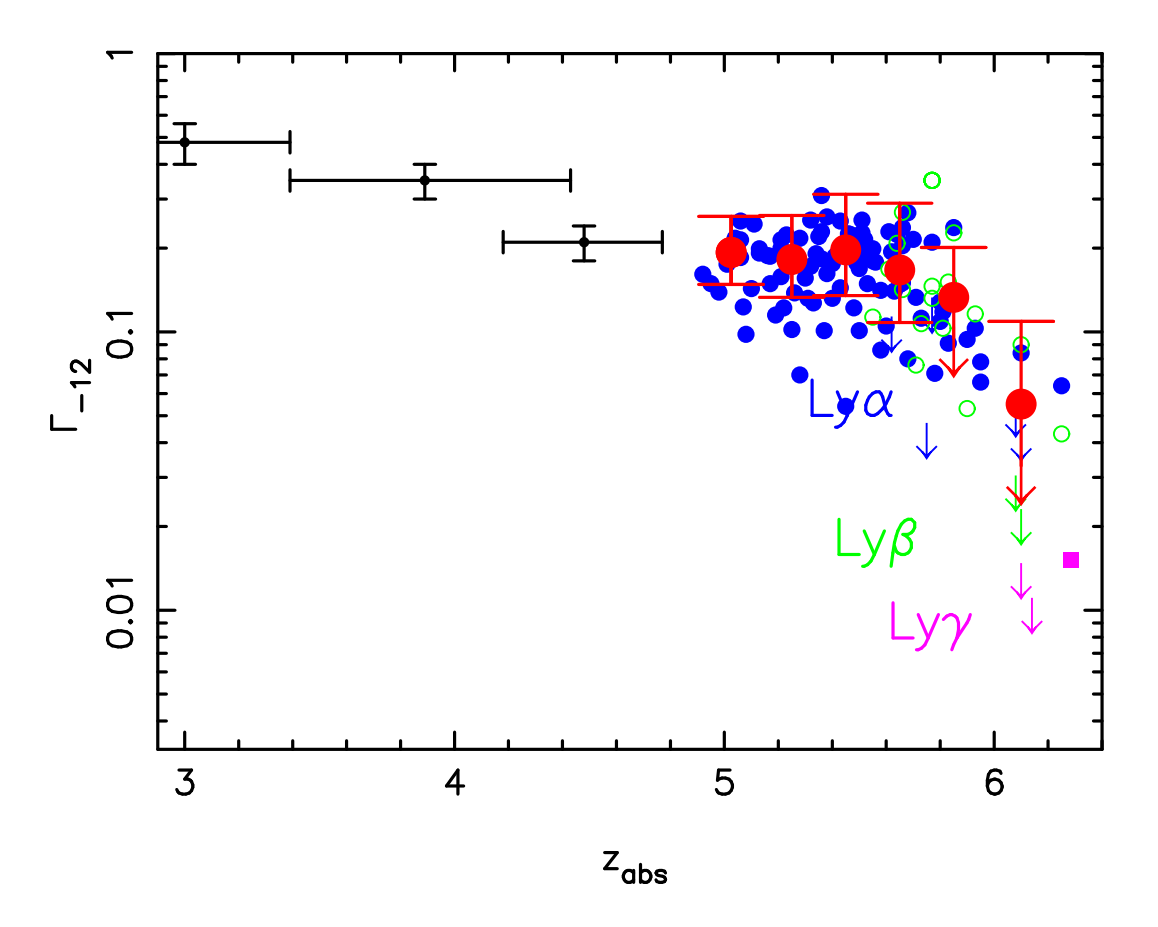


Fig. 6.— Evolution of the photoionization rate (in units of $10^{-12}~\rm s^{-1}$) with redshift. The points at $z_{\rm abs} < 4.8$ are taken from McDonald & Miralda-Escudé (2001). For the highest redshift points, measurements using Ly α (closed symbols) and Ly β (open symbols) transitions are shown separately. Large, solid symbols with error bars are the average and 1- σ dispersion of Γ at high redshift. As in Figure 5, we show the Ly γ measurements, but do not include them in the calculation of average and dispersion in the highest redshift bin.

where $\tilde{W}(x) \equiv \sin x/x$ is the top-hat window function, and $\langle \tilde{F}_k^2 \rangle$ is the one-dimensional power spectrum, related to the normal three-dimensional linear power spectrum as (Kaiser & Peacock 1991):

$$\langle \tilde{F_k^2} \rangle = \frac{1}{2\pi} \int_k^\infty P(y) y dy.$$
 (13)

Using the linear power spectrum determined from the Ly α forest at $z \sim 3$ by McDonald et al. (2005), and assuming that it grows linearly with scale factor at high redshift, we find that at $z \sim 6$, the one-dimensional r.m.s. density fluctuation is $\sigma_m(L) = 0.11$ over $\Delta z = 0.15$. From Eq. (7), $\Gamma \propto \rho_b^2$ for a given optical depth; a 10% fluctuation in the average density leads to a fluctuation of $\sim 20\%$ in the resulting Γ value. This value is somewhat smaller than the dispersion of the Γ measurements at $z \sim 5$, and is much smaller than that at higher redshift. Over such a narrow redshift range, the average IGM temperature is not likely to have changed by more than a factor of two (Hui & Haiman 2003), resulting in a difference in estimated Γ by < 60%, since $\tau \propto \alpha(T)/\Gamma \propto T^{-0.7}/\Gamma$ (§3.2). Therefore, we interpret the large dispersion of optical depth and derived ionizing background at z > 5.7 as a result of fluctuations in the UV background near the end of reionization: even over the scale size of 44 h⁻¹ comoving Mpc, the average UV background fluctuates by a factor of $\gtrsim 4$. The dispersion of estimated Γ values at z < 4 is much smaller and is mostly due to sample variance of the average density along the line of sight.

Large fluctuations in the UV background also imply that the transmission is correlated over large scales. We calculate the line of sight dispersion of transmitted flux by comparing the average transmitted flux over neighboring bins along the same line of sight, and subtract from it the difference due to redshift evolution (Eq. 5). We find that at $z \geq 5.5$, when averaging over redshift interval $\Delta z < 0.1$, the dispersion of line of sight of GP optical depth is $\sim 20\%$ smaller than the dispersion when comparing different lines of sight. Thus the GP optical depth is correlated over scales of tens of comoving Mpc. At $\Delta z > 0.15$, this difference is < 10%. At larger Δz , the test becomes difficult due to the limited line of sight towards any particular quasar. Because of the limited sample size, non-uniform S/N of the sample spectra, and strong redshift evolution, we do not attempt to calculate the transmission two-point correlation function in this paper (e.g. McDonald et al. 2000). By observing high-redshift quasar pairs that have projected separations of tens of comoving Mpc, one could check this correlation in the transverse direction (e.g. Mahabal et al. 2005).

Large fluctuations in the UV background are a generic feature of the IGM close to the end of reionization, when the individual HII regions start to percolate and most of the UV photons come from the earliest highly clustered star forming galaxies. Note that in our photoionization model, we assumed a uniform UV background. Here we show that at the end of reionization, there is a large background fluctuation. The derived UV background fluctuations will provide a sensitive test of models of the reionization history when compared directly with simulations.

4.2. Neutral Fraction and Mean Free Path of the IGM

We use the GP optical depth measured in \(\)3 and the IGM density distribution, Eq. (9), to calculate both the volume- and mass-averaged neutral hydrogen fraction. Figure 7 shows the estimated volume-averaged neutral fraction using our sample of nineteen quasars. It is compared with a recent simulation by Gnedin (2004), which has a sharp transition in the ionization state at $z \sim 5.5 - 6.5$, and a small total Thompson scattering optical depth to CMB $\tau_e = 0.06$ (compare to the WMAP three-year value of $\tau_e = 0.09 \pm 0.03$, Spergel et al. 2006, see §4.3 for more discussion on the model comparisons). The strong evolution of neutral fraction in Paper I is confirmed here: there is an order of magnitude increase between $z \sim 5.1$ and 6.1, with the evolution accelerated at z > 5.7. We emphasize that the calculation of volume- or mass-averaged neutral fractions depends on the density distribution function of the IGM as well as on the assumption of a uniform UV background. Oh & Furlanetto (2005) show that most of the IGM transmission is through the most highly ionized, underdense regions (see also Figure 7 of Paper I). As discussed in Paper I, the volume averaged values are less affected by the ionization state of high-density regions than are the mass averaged values. Over a narrow redshift range where the density distribution of the IGM evolves little, the ratio of neutral fractions at different redshifts is a robust quantity, especially when compared with simulations.

In Paper I, we calculated the evolution of the mean free path of ionizing photons, using the model of Miralda-Escudé, Haehnelt, & Rees (2000). They model reionization using the evolution of critical overdensity Δ_i , above which the IGM is still mostly neutral, and below which it is mostly ionized. Δ_i increases as the reionization front progresses to higher density regions. They also suggest an expression for the ionizing photon mean free path: $\lambda_i = \lambda_0 [1 - F_v(\Delta_i)]^{-2/3}$, where $F_v(\Delta_i)$ is the fraction of volume with $\Delta < \Delta_i$, and $\lambda_0 H = 60$ km s⁻¹, which assumes that the shapes of isolated density contours remain roughly constant as Δ_i decreases. However, the critical overdensity Δ_i is not well defined in the simple photoionization picture; we assumed that 95% of the total neutral gas lies above Δ_i in Paper I. In addition, overdense regions in the IGM are likely to contain the earliest star-forming galaxies that provide most of the ionizing photons, thus they might have been ionized earlier. For these reasons, in this paper, we propose an alternative approach to calculate the mean free path λ by simply using the mass averaged neutral hydrogen density:

$$\frac{1}{\lambda} = \langle \sigma_{\nu} \rangle \frac{\int_{0}^{\Delta_{c}} n_{\rm HI}(\Delta) p(\Delta) d\Delta}{\int_{0}^{\Delta_{c}} p(\Delta) d\Delta},\tag{14}$$

where $\langle \sigma_{\nu} \rangle$ is the frequency averaged cross section of Lyman limit absorption, assuming an ionizing spectrum $J_{\nu} \propto \nu^{-5}$ (Barkana & Loeb 2001), and $n_{\rm HI}(\Delta)$ is the neutral fraction corresponding to a certain overdensity calculated using Eqs. (7) - (9). The integrals over the density distribution are only carried out to $\Delta_c = 150$, above which the region is already virialized and is no longer part of the IGM. This expression is accurate in cases in which the mean free path is larger than the scale of IGM clustering, or the UV photon field follows the IGM density distribution; these assumptions might not be valid at the early stage of reionization. Furthermore, these calculations depend

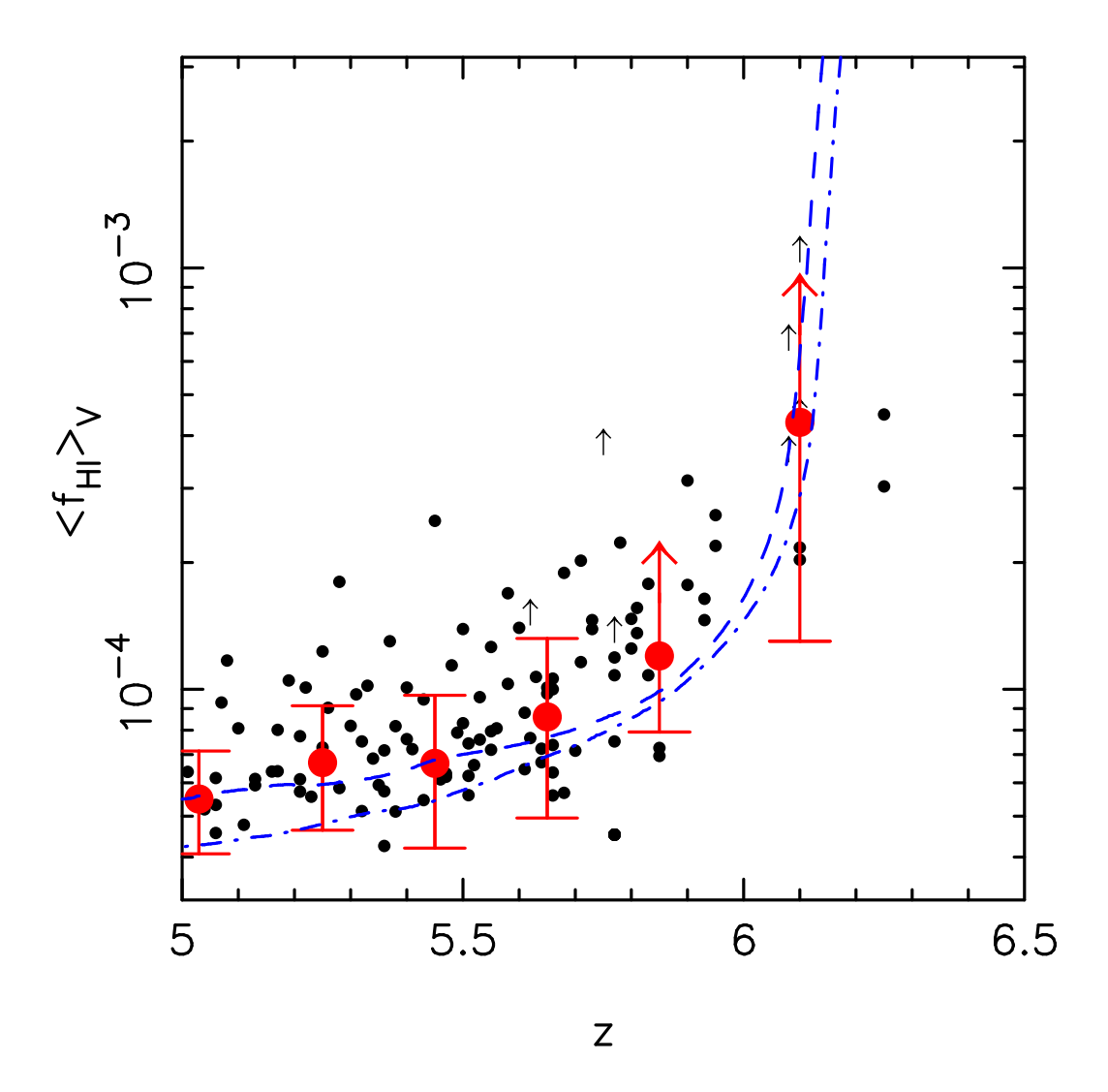


Fig. 7.— Evolution of volume-averaged neutral hydrogen fraction of the IGM. The small dots are measurements based on the nineteen high-redshift quasars, while the large points with error bars are the means in bins of redshift. The dashed and dotted-dashed lines are the volume-averaged results from the simulation of Gnedin (2004) with box sizes of 4 $\rm h^{-1}$ Mpc and 8 $\rm h^{-1}$ Mpc, respectively.

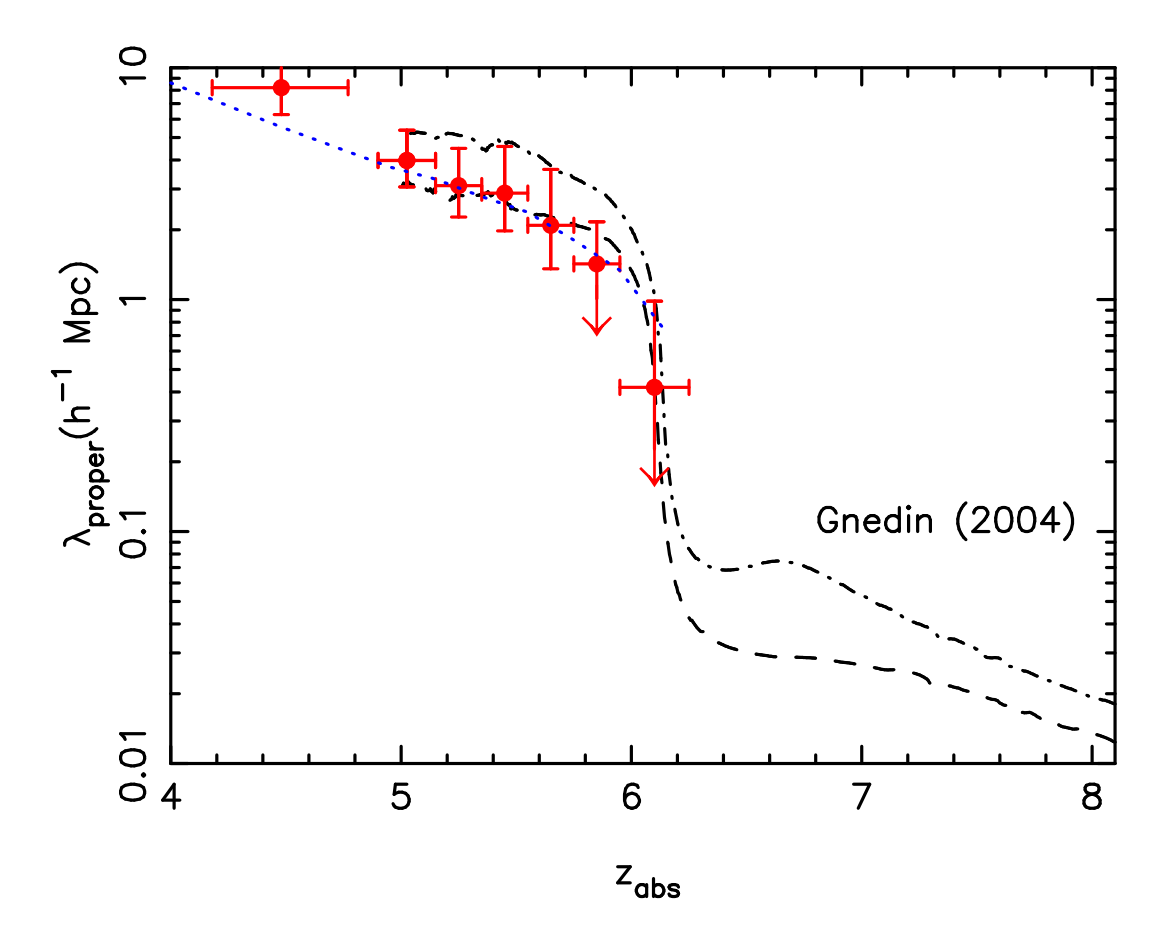


Fig. 8.— Evolution of the mean free path of ionizing photons inferred from the observations using Eq. (13) (solid symbols with error bars) and using the method presented in Paper 1 (dotted line), compared with simulations of Gnedin (2004, dashed and dashed-dotted-dashed lines). The mean free path at $z\sim5.7$ is comparable to or smaller than the correlation length of high-redshift star forming galaxies.

on the derived neutral fraction and assumed IGM density distribution. While the exact values of the mean free path are model-dependent, the strong evolutionary trend is clearly detected. Figure 8 shows the mean free path calculated using Eq. (14), where both the mean and 1- σ error bars are presented. The dotted line shows the mean free path calculated using the method in Miralda-Escudé et al. (2000) and in Paper I. The two results are fully consistent. They again show the accelerated transition at $z_{abs} > 5.7$, where only an upper limit can be derived for complete GP trough regions.

At z > 5.7, the mean free path is smaller than $0.5 \ h^{-1}$ proper Mpc (3.5 h⁻¹ comoving Mpc). In comoving units, this is comparable to the correlation length of galaxy clustering at $z \sim 0$, $(r_0 \sim 5 \ h^{-1}$ Mpc, Zehavi et al. 2005), and of Lyman break galaxies at $z \sim 2-4$ $(r_0 \sim 4 \ h^{-1}$ Mpc, Adelberger et al. 2005), and at z = 4-5 $(r_0 \sim 4-8 \ h^{-1}$ Mpc, Kashikawa et al. 2006). At z > 5, evidence of galaxy clustering on scales of ~ 10 Mpc are reported in Hu et al. (2005), and Malhotra et al. (2005). High-redshift star forming galaxies, which likely provide most of the UV photons for reionization, are highly biased and clustered at physical scales similar to the mean free path. The assumption of uniform UV background under which we have derived these results is no longer valid. We saw clear evidence for non-uniform Γ in §4.1.

4.3. Comparison with Hydrodynamical Simulations

Hydrodynamical simulations (Gnedin 2002, 2004, Razoumov et al. 2002, Paschos & Norman 2005) have been used to calculate the evolution of the GP optical depth during the epoch of reionization. Gnedin (2004) presented a SLH simulation of reionization by stellar sources with a new recipe for radiative transfer using an optically thin variable Eddington tensor approximation and box sizes of 4-8 h⁻¹ comoving Mpc. In these simulations, the mean mass-averaged neutral fraction reaches 10^{-2} and 0.5 at z=6.3 and 7.3, respectively. The reionization process is modelled as similar to a phase transition, completed within $\Delta z \sim 1$. Similarly, Paschos & Norman (2005) presented a set of reionization simulations using the Eulerian code, Enzo, and a box size of 6.8 h⁻¹ co-moving Mpc. Their default model has a sharp reionization at $z_{\rm reion} \sim 7$, around which the mass-average neutral fraction increases from 10^{-3} to of order unity. Both simulations have been calibrated according to the average GP optical depth measurements at z < 6 using earlier datasets (e.g. Becker et al. 2001, Songaila 2004), so the consistency in measurements in this redshift range is by design.

However, these simulations which model the reionization process as a phase transition could be too simplistic for two reasons. First, both simulations include only a simple prescription of the evolution of emissivity of ionizing sources. The simulations have not captured all the relevant physics, especially the effects of early galactic feedback and large scale structure. The total Thompson scattering optical depth (τ_e) is less than 0.10 in both simulations, inconsistent with the WMAP first-year measurements at face value ($\tau = 0.17 \pm 0.06$, Kogut et al. 2003, Tegmark et al. 2004), but is consistent with the WMAP three-year measurements (Spergel et al. 2006). A number

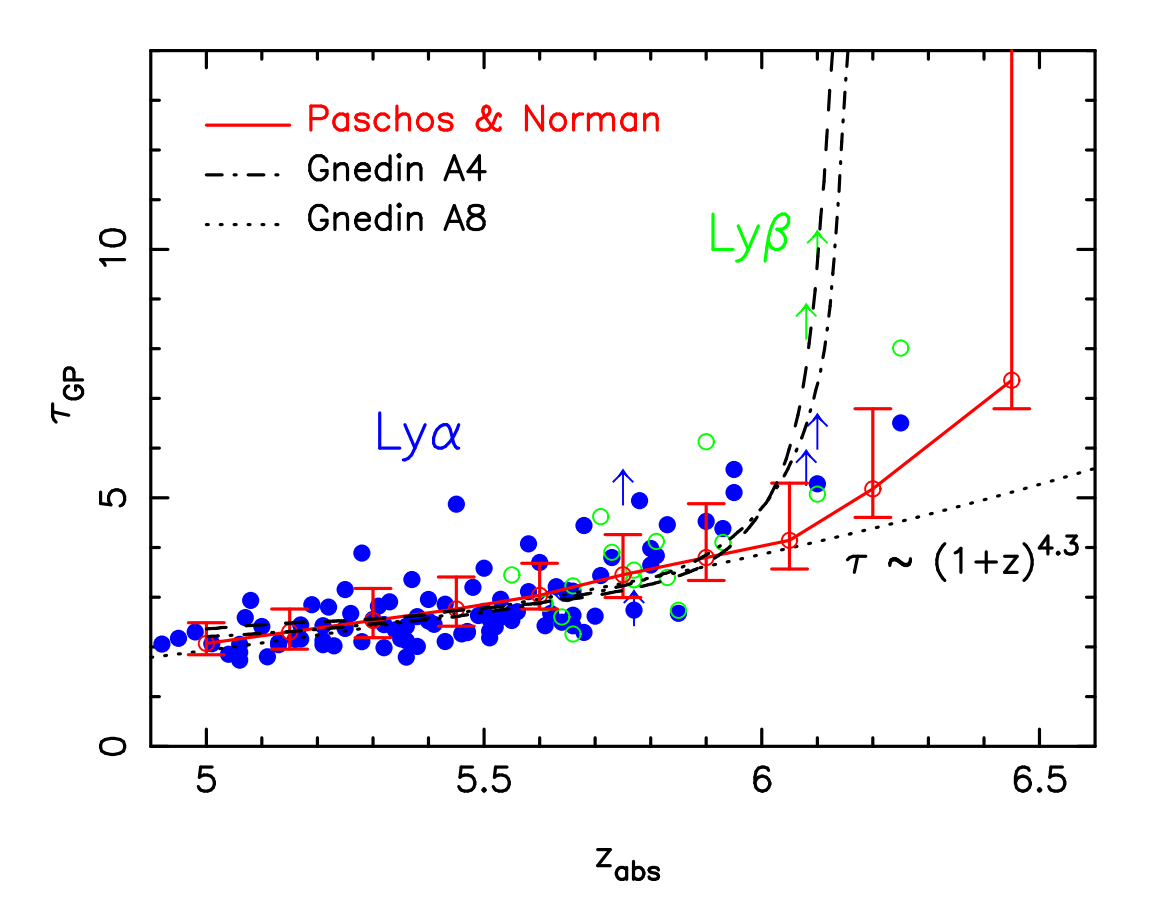


Fig. 9.— Comparison of the evolution of observed GP optical depth with simulations. Data points are the same as in Figure 5. The dotted line is the power-law fit to optical depth evolution at z < 5.5: $\tau_{\rm GP} \propto (1+z)^{4.3}$. The solid line with error bars is the result from simulations of Paschos & Norman (2005), which have $z_{\rm reion} \sim 7$. The dashed and dotted-dashed lines are the 4 Mpc and 8 Mpc simulations of Gnedin (2004), which have $z_{\rm reion} \sim 6.5$. The data points fall between the two simulations, but are somewhat closer to those of Gnedin.

of semi-analytical analyses (e.g., Cen 2003a,b, Chiu et al. 2003, Wyithe & Loeb 2003a, Haiman & Holder 2003 etc.), show that adding feedback from an early generation of galaxy formation, or adjusting the star formation efficiency at z > 6 - 10, will produce a prolonged, or multi-epoch reionization history. These models predict a GP optical depth consistent with quasar observations at z < 6.5, while having a large total Thompson scattering optical depth.

The second problem is the impact of large scale structure. Both simulations have a limited box size (< 10 comoving Mpc). However, Wyithe & Loeb (2004) and Furlanetto & Oh (2005) have studied growth of ionized bubbles at the end of reionization, and estimated that the bubble have sizes of > 10 Mpc at the end of the overlapping phase. Wyithe & Loeb (2004, 2005) showed that the observed redshift of overlap along different lines-of-sight has a variation of $\Delta z \sim 0.15$, and the GP optical depth variations should be of order unity on a scale of \sim 100 comoving Mpc. These results are consistent with the large scale variation of the UV background discussed in §4.1. Thus to fully understand the reionization process, simulations with box sizes of the order 100 Mpc are needed (e.g., Kohler et al. 2005).

Figure 9 compares the GP optical depth measurements of Figure 5 with the simulations of Gnedin (2004) and of Paschos & Norman (2005). We also compare the estimated IGM neutral fraction and mean free path of UV photons with those of the Gnedin simulations in Figures 7 and 8. In the simulations, the onset of reionization is characterized by an acceleration in the evolution of the GP optical depth. Paschos & Norman (2005) showed that when $z_{\rm reion} - z > 1$, the GP optical depth scales as a simple power-law $\tau_{\rm GP} \propto (1+z)^{4.2}$, consistent with what we find at $z_{abs} < 5.7$. For the last $\Delta z = 0.5 - 1$, as the epoch of reionization approaches, the optical depth evolution accelerates, again mirroring the observed trend. The observed points fall in the range covered by the three simulations. A similar rapid change is noted in the volume-averaged neutral fraction (Figure 7) and photon mean free path (Figure 8), in which the simulations closely match the values estimated from observations.

The simulations also show that the end of reionization is accompanied by a rapid increase of dispersion in optical depth. Paschos & Norman (2005) calculated the flux variance among different lines of sight by observing through random lines of sight in the simulation box. The solid error bars in Figure 9 are the 68% range of the optical depth measurements at each redshift bin. At z < 5.5, the dispersion in the simulation matches the observations well. It also reproduces the trend of increased scatter at z > 6, although at somewhat higher redshift. This accelerated evolution corresponds to the stage of reionization where individual HII regions begin to overlap and the IGM ionization experienced a rapid transition (e.g. Gnedin 2002). The comparison of the observations with simulations strongly suggest that $z \sim 6$ corresponds to the end of the overlapping stage of reionization, but for reasons mentioned earlier, it does not provide detailed guidance to what happened at much higher redshift, when the reionization history may have been more complex.

5. Distribution of Dark Gaps

In the last three sections, we have used the evolution of the effective optical depth to probe the ionization state of the IGM. The effective optical depth directly probes the neutral fraction and UV ionizing background in photoionization models. However, it is a low order statistic. At z > 5, the appearance of the Ly α forest is the reverse of that at low redshift: most regions along the line of sight are optically thick, while a small fraction of transparent "spikes" provide most of the Ly α transmission. Meanwhile, ever longer dark absorption gaps – continuous regions with large optical depth – emerge at $z_{abs} > 5.7$. A successful theory of IGM evolution at the end of reionization needs to reproduce not only the evolution of the mean optical depth, but also the geometry and topology of IGM transmission and the dark gaps. In Pentericci et al. (2002) and in Paper I, we examined the distribution of transparent spikes along a few lines of sight. In this section, we expand these previous studies and discuss three issues: the presence of complete GP absorption troughs at the highest redshift (§5.1); the evolution of the dark gap distribution (§5.2); and the use of dark gap lengths to constrain the IGM neutral fraction (§5.3).

5.1. Gunn-Peterson Troughs in the Highest-Redshift Quasars

The presence of complete Gunn-Peterson troughs is the most compelling evidence that the IGM is approaching the end of the reionization epoch at $z \sim 6$. To probe the evolution of the IGM at z > 6 requires quasars at z > 6.1 to not be affected by the quasar proximity effect. Figure 11 shows the regions immediately blueward of the Ly α and Ly β emission lines for the five quasars in our sample at z > 6.1; deep absorption troughs with $\tau_{\rm GP}^{\rm eff} > 5$ and length $\Delta z > 0.1$ are indicated. The ends of troughs are chosen as locations at which significant transmission spikes with $\tau < 2.5$ are detected. Table 6 summarizes the GP optical depth measurements for these troughs. We now briefly discuss the case for each quasar:

SDSS J1148+5251 (z=6.42). This object is discussed in detail in White et al. (2003, 2005) and Oh & Furlanetto (2005). Extended dark regions in Ly α absorption start at $z_{abs} > 5.91$; however, the spectrum shows clear transmissions in the Ly α - Ly γ transitions at this redshift. White et al. (2003) speculated that the Ly β transmission could be due to Ly α emission from intervening galaxies at $z \sim 4.9$, as suggested by strong CIV absorption at that redshift. Subsequent HST imaging indicated that the flux in the Ly β trough is a point source coincident with the quasar position, inconsistent with the intervening galaxy hypothesis. The Ly α and Ly β troughs yield consistent optical depth measurements: $\tau_{\rm GP}^{\rm eff} \sim 5.5 - 7$. The consistency between the Ly α and Ly β GP optical depth measurements is direct evidence that at $z \sim 6$, the IGM is already highly ionized at least along this line of sight, although the neutral fraction has increased by a factor of ~ 4 from that at $z \sim 5.7$ even in this most transparent line of sight among z > 6.1 quasars. Table 4 also shows the Ly γ measurements in the highest-redshift interval at z = 6.25 - 6.32, where the transmission is detected at $3-\sigma$ level, yielding an effective optical depth: $\tau_{\rm GP}^{\rm eff} \sim 15$. No Ly α or Ly β

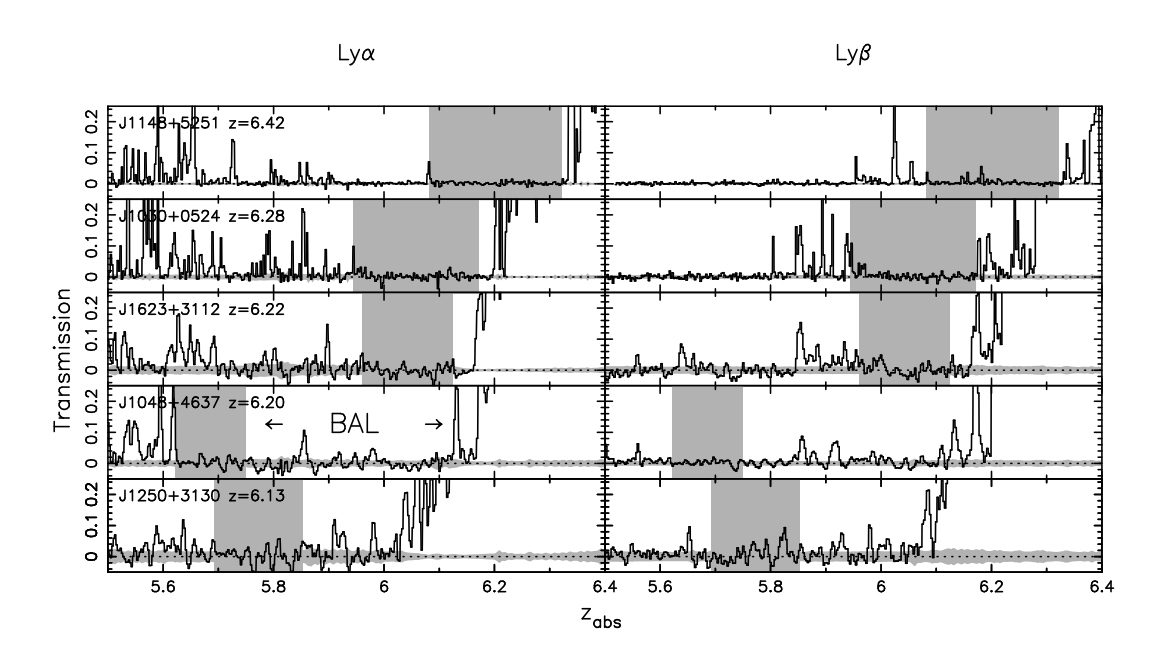


Fig. 10.— Deep GP troughs in the five highest-redshift quasars known at z > 6.1, in both the Ly α and Ly β transitions. The grey band around zero transmission represents the 1- σ uncertainty of the data. The ends of troughs are chosen as locations at which significant transmission spikes are detected. SDSS J1048+4637 is a BAL quasar, in which we use the redshift of the CIV BAL feature as the upper bound of the GP trough. These quasars show significant line of sight variation in the GP optical depth measurements and the redshift where deep troughs first appear.

transmission is detectable over this narrow redshift range, consistent with the Ly γ measurement, and suggesting large fluctuations in the neutral fraction along the line of sight. Note that there is also a long Ly α trough at 5.91 < $z_{\rm abs}$ < 6.08, although it has clear transmission in Ly β , indicating a high level of ionization.

SDSS J1030+0524 (z = 6.28). This is the first quasar at z > 6 in which a complete GP trough was detected (Becker et al. 2001); it still has the longest and deepest absorption trough among known quasars, in which no flux in any of the Lyman transitions is detected, yielding the most stringent constraint on the evolution of the neutral fraction.

SDSS J1623+3112 (z = 6.22). This line of sight is very similar to that of SDSS J1030+0524, with complete GP troughs in the Ly α and Ly β transition immediately blueward of the emission lines. The starting redshift and length of the complete GP trough are also similar. This object is fainter and has a shorter total exposure time, yielding an upper limit 15% weaker than that of SDSS J1030+0524. It also has a Ly γ trough with no detectable transmission.

SDSS J1048+4637 (z=6.20). This is a BAL quasar (Fan et al. 2003, Maiolino et al. 2004). The SiIV absorption extends to $z_{abs} \sim 5.83$, and a somewhat weaker CIV trough reaches to $z_{abs} = 5.75$. We therefore can only measure the IGM properties at lower redshift. The quasar has a dark trough at z=5.63-5.75, where no flux is detected in either Ly α or Ly β at a level comparable to SDSS J1623+3112. This is at a redshift considerably lower than the other lines of sight. We regard it as less reliable, as the trough could be affected by weaker BAL features as well as by absorption troughs from other ions (e.g. PV λ 1121, Arav et al. 2001).

SDSS J1250+3130 (z=6.13). This object shows a dark Ly α GP trough at z=5.69-5.85 with an optical depth $\tau_{\rm GP}^{\rm eff}>4.6$ (2- σ). The trough doesn't start immediately blueward of the Ly α emission line, and has detectable Ly β transmission, with $\tau_{\rm GP}^{\rm eff}\sim6.5$. The Ly β measurement is comparable to that of SDSS J1148+5251 at considerably higher redshift, although the S/N of the spectrum is lower for this quasar.

The properties of these absorption troughs show significant variation between lines of sight. Two of the three quasars at z>6.2 show complete Ly α - Ly γ troughs, while the third one has only a somewhat higher optical depth than seen at lower redshift. On the other hand, some dark troughs already start to appear at $z\sim5.7$. We quantify the evolution of the dark absorption gaps in the next subsection.

5.2. Dark Gap Distribution

Statistics of dark gaps (e.g. Croft 1998) were first applied to a sample of z=4-6 quasars by Songaila & Cowie (2002). They studied the evolution of continuous absorption gaps with large optical depth ($\tau > 2.5$) and found that extended absorption troughs such as those observed by Becker al. (2001) in SDSS J1030+0524 can be explained by large variations in the UV background

at z > 6. Barkana (2002) presented a semi-analytic model for the length of dark gaps as a function of IGM HII region filling factor. Furlanetto, Hernquist, & Zaldarriaga (2004) also presented a model of dark gap distribution, considering source clustering and the inhomogeneous IGM. Paschos & Norman (2005) and Kohler et al. (2005) studied the dark gap distribution using spectra derived from their hydrodynamical simulations. They suggest using the distributions of dark gaps as a statistic to compare with observations, and found that the onset of reionization is associated with a dramatic increase both in the average and dispersion of gap length.

Figure 11 shows the distribution of Ly α dark gap lengths in the 12 lines of sight that have Keck/ESI spectra. We define dark gaps as continuous regions in the quasar spectra in which all pixels have optical depth larger than a threshold τ_{\min} . In the upper panel of Figure 11, we use $\tau_{\rm min}=2.5$, the same as that of Songaila & Cowie (2002) and Paschos & Norman (2005). Both the average gap length and its dispersion increase dramatically at z > 5.7. At this optical depth threshold, dark regions with $\Delta r \gtrsim 40$ comoving Mpc already begin to appear at $z_{abs} \sim 5.3$ (e.g. Djorgovski et al. 2001). Long gaps with $\Delta r \gtrsim 80$ comoving Mpc appear at $z_{abs} \sim 5.7$; however, they are relatively rare while most lines of sight still have plenty of pixels with $\tau < 2.5$ and only short dark gaps. At $z_{abs} > 5.9$, all lines of sight have long dark gaps with $\tau > 2.5$. In many cases, the gap length is only a lower limit, as the gap extends all the way to the quasar proximity zone. Note that at the high redshift end, imperfect sky subtraction in regions with strong OH lines results in large residuals in the spectrum and an underestimate of the dark gap length. This transition from isolated, short gaps occupying only a small fraction of pixels, to deep, long troughs is the most abrupt transition among all the IGM properties we have presented in this paper, and is difficult to explain by a gradual thickening of the Ly α forest. Rather, it suggests a phase transition in the IGM geometry. Detailed comparison with state-of-art simulations will constrain the IGM geometry at this critical stage of reionization.

Figure 11 compares the observations with the simulations of Paschos & Norman (2005) described in §4.3. The dashed and dotted lines are model predictions of the average gap length for spectral resolution of R = 5300 and R = 36000. Our spectra are binned to R = 2600, and should be compared to their low-resolution results. The observations and simulations agree very well at z < 5.5. Both also show a strong break in the evolution of dark gap length; however, the break in the observations is both earlier (by $\Delta z \sim 0.5$) and sharper. This is consistent with the comparison in Figure 9, and suggests that the reionization epoch is at somewhat lower redshift than in the simulations. Note, however, the simulation of Paschos & Norman (2005) has a box size of only 6.8 h⁻¹ comoving Mpc. They used multiple passes through the box to measure the gap sizes larger than the box size, which could bias the result.

At $\tau_{\rm min}=2.5$, all gaps at z>6.0 are longer than 100 comoving Mpc, and most are only lower limits. In order to further constrain the neutral fraction, we use a higher optical depth threshold $\tau>3.5$ (shown in the lower panel of Figure 11). Even at z>6.0, the average length of dark gaps is still finite: $\Delta r \gtrsim 80$ comoving Mpc. At this higher threshold, it is clear that the IGM is not yet neutral at $z\sim6$.

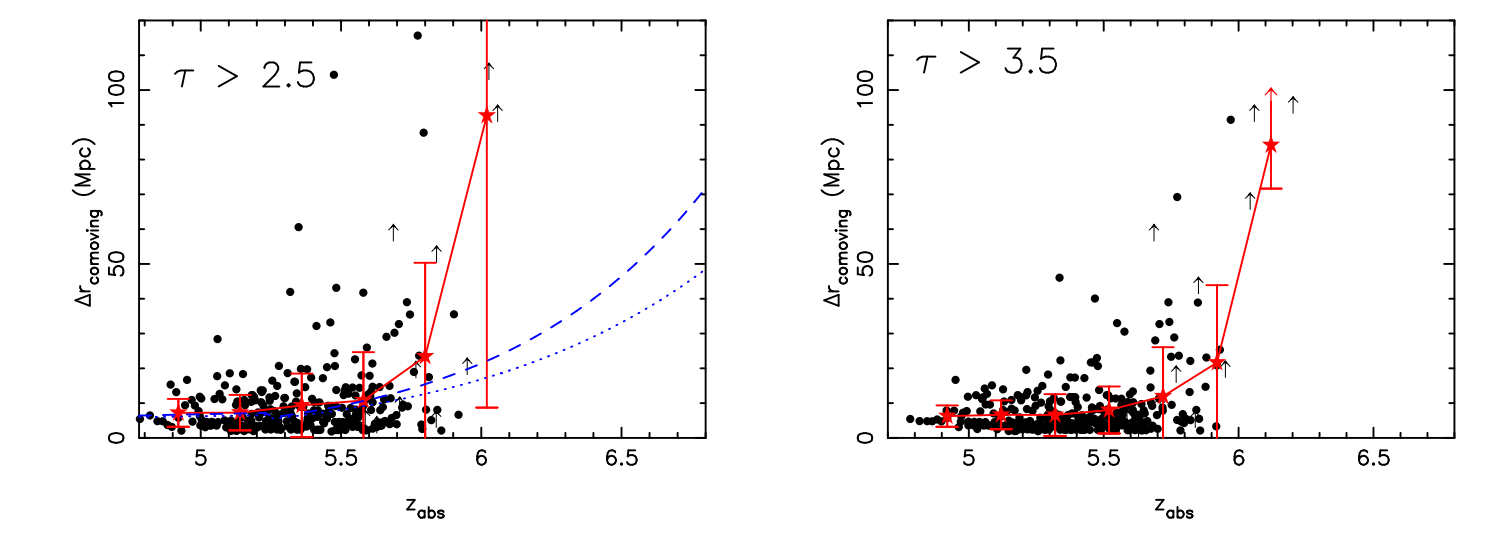


Fig. 11.— Distributions of dark gap lengths, defined as continuous regions in the spectra in which all pixels have observed optical depth larger than 2.5 (upper panel) and 3.5 (lower panel) for the Ly α transition in the twelve lines of sight that have Keck/ESI observations. Upward arrows are gaps immediately blueward of the quasar proximity zone, therefore the length is only a lower limit. Solid lines with error bars are mean depth lengths, with 1- σ dispersion given at each redshift bin. Long dark gaps start to appear at $z \sim 5.6$, and the average gap length increases rapidly at z > 5.9. In the upper panel, we also compare the observations with simulations of Paschos & Norman (2005), which has a sharp reionization at $z \sim 7$. The dashed and dotted lines are for spectral resolution of 5300 and 30000, respectively, in the simulated spectra. The observed spectra are binned to $R \sim 2600$. The observations appear to have reached the overlap stage at $z \sim 6$.

In the redshift range considered in this paper, the measurement of the dark gap distribution and the GP optical depth place similar constraints on the ionization of the IGM. However, at $z_{\rm abs} > 6.5$, it will become increasingly difficult to map the reionization history using the GP optical depth. Currently, with ~ 10 hours of observing time on 10-meter class telescopes, we are able to place lower limits on the GP optical depths of $\tau \lesssim 7$ using Ly α , and a factor of ~ 2 better using Ly β and Ly γ , corresponding to a neutral fraction of $10^{-2} - 10^{-3}$. It is difficult to improve this measurement further in practice, because the optical depth limit depends logarithmically on the observing time and the ability to control sky subtraction systematics. At z > 6, most of the pixels are completely dark, and contain little information. After entering the redshift range where continuous dark gaps dominate, all useful information is contained in the flux and distribution of few remaining transmitting pixels. Therefore, the dark gap distribution provides a powerful alternative to map the IGM ionization at high neutral fraction. Paschos & Norman (2005) show that even when the average neutral fraction is of the order few tenths, the average gap length is still finite, due to the presence of regions that had already been ionized by star forming galaxies. In the next subsection, we place an upper limit on the neutral fraction using the finite length of the gaps.

5.3. Constraining the Neutral Fraction with Gap Statistics

So far in this paper, we have only considered a photoionized IGM without explicitly taking into account the presence of strong UV ionizing sources that caused reionization: early star forming galaxies and AGNs. These objects create expanding HII regions even in a largely neutral IGM, and result in transmitting spikes in the absorption spectrum. However, in a neutral IGM, the optical depth at the Ly α resonance line center is so large that it generates an extended GP damping wing (Miralda-Escudé 1998). Small HII regions are still optically thick to the observer due to absorption from this damping wing; and only large HII regions around long-lived, luminous sources can survive the damping wing absorption. Therefore, the existence of transmitting regions between dark gaps, together with a model for the ionizing sources, can be used to place an upper limit on the IGM neutral fraction independent of other IGM optical depth constraints. This is similar to the constraint using the evolution of Ly α emitting galaxies (Malhotra 2005, Stern et al. 2005, Haiman & Cen 2005, Santos 2005). In the case of Ly α galaxies, a neutral IGM will significantly attenuate their Ly α flux. Therefore, the lack of evolution in the Ly α galaxy luminosity function is used to put an upper limit on the IGM neutral fraction $\lesssim 50\%$ at $z \sim 6.5$.

Haiman (2002) gives the radius of an HII region R_s in a uniform IGM with neutral fraction $f_{\rm HI}$ around a star forming galaxy with star formation rate of \dot{M}_* ,

$$R_s = 0.65 \left(\frac{\dot{M}_*}{40 \text{ M}_{\odot} \text{yr}^{-1}} \right)^{1/3} \left(\frac{t_*}{10^7 \text{yr}} \right)^{1/3} f_e^{1/3} f_{\text{HI}}^{-1/3} \left(\frac{1+z}{7} \right)^{-1} \text{proper Mpc}, \tag{15}$$

where t_* is the duration of the starburst, and f_e is the escape rate of Lyman Limit photons.

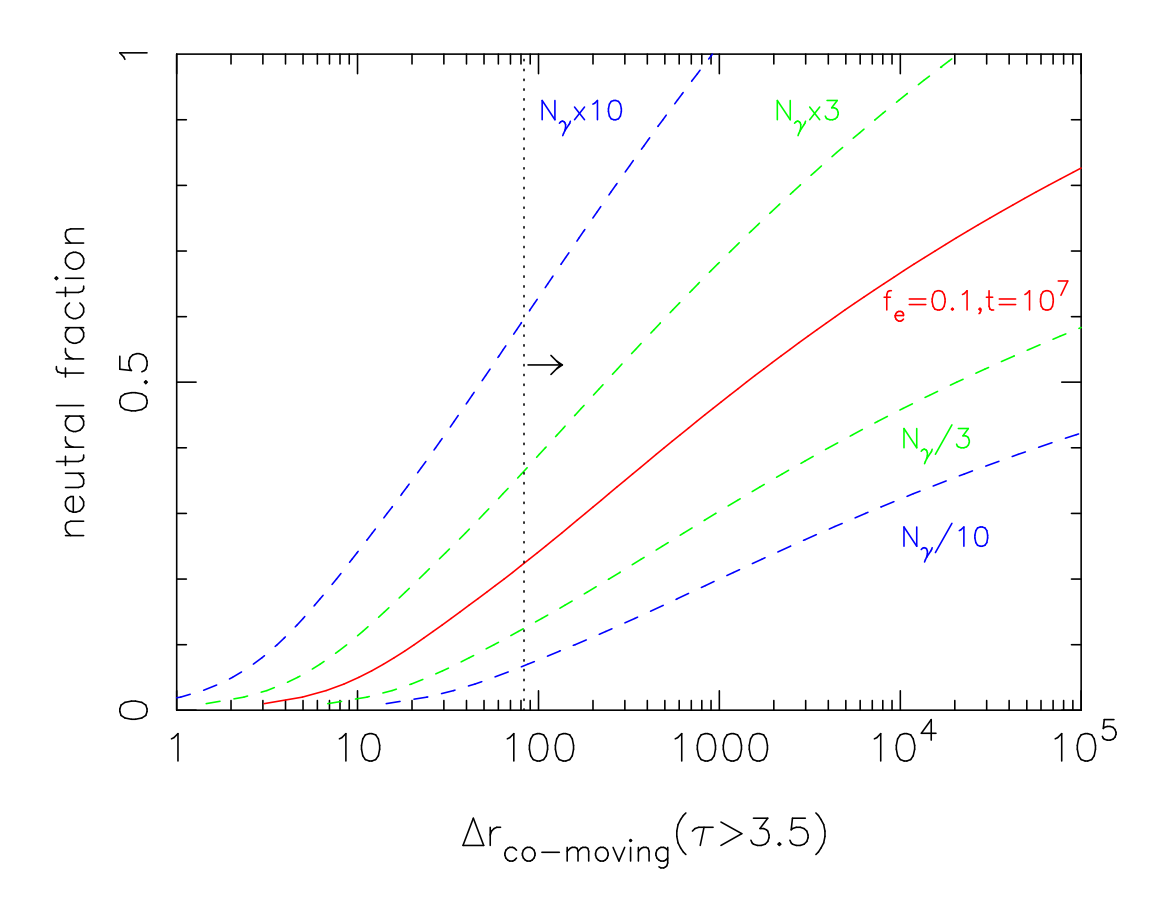


Fig. 12.— Average length of dark gaps with $\tau > 3.5$ as a function of IGM neutral fraction, assuming that transmitting regions in the quasar spectrum are generated by HII regions surrounding early star forming galaxies which follow the Yan & Windhorst (2004b) luminosity function. The solid (red) curve is the default case where the duration of star formation in each galaxy is 10^7 yr and the escape fraction of ionizing photons is 10%. The two groups of dashed curves above and below the default case correspond to the number of escaping photons 3 and 10 times larger or smaller than the default case. The dashed line is the observed limit on the average dark gap length at $z \sim 6$, consistent with a neutral fraction $\lesssim 0.5$.

For such an HII region, the GP damping wing optical depth at a distance r from the center of the galaxy is approximately (Cen 2003c):

$$\tau_d(r) = 1.2 f_{\rm HI} \left(\frac{R_s - r}{1 \text{ Mpc}}\right)^{-1} \tag{16}$$

at large distances from the center of the resonant Ly α line. In order to preserve a dark gap threshold $\tau_{\rm min} > 3.5$, we require the center of the galaxy HII region to have an optical depth from the damping wing, $\tau > 3.5$. For a neutral IGM $f_{HI} = 1$, we have $R_s = 0.34$ Mpc, corresponding to a star forming rate of $\dot{M}_* \sim 70~\rm M_{\odot} yr^{-1}$ using Eq. (15), assuming that the duration of star formation is $t_* = 10^7$ yr and the escape fraction is $f_e = 0.1$ (Steidel et al. 2001). This is a luminous galaxy at $z \sim 6$: using the calibration of Bunker et al. (2004), it has a z_{AB} magnitude of 24.3. Such galaxies are extremely rare at $z \sim 6$ and are not likely to generate transmitting spikes every ~ 100 comoving Mpc. The fact that the gap length is ~ 100 Mpc therefore already rules out a completely neutral IGM. To include the contribution of faint galaxies and place a more stringent constraint on the neutral fraction, we assume a luminosity function of star forming galaxies at $z \sim 6$ following Yan & Windhorst (2004b):

$$\Phi(M_{1300}) = 0.921\Phi_* 10^{-0.4(\alpha+1)(M_{1300}^* - M_{1300})} \exp[-10^{0.4(M_{1300}^* - M_{1300})}], \tag{17}$$

where $\Phi_* = 4.55 \times 10^{-4} \mathrm{Mpc^{-3}}$, $\alpha = -1.6$ is the faint end slope of the luminosity function, M_{1300} is the absolute AB magnitude at rest-frame wavelength 1300Å, and the characteristic luminosity $M_{1300}^* = -21.03$. The average length of the dark gap is then the distance between two star forming galaxies that have $\tau < 3.5$ at the center of their respective HII regions:

$$\langle 1/\Delta r \rangle = \int \Phi(M_{1300}) \pi r_{3.5}^2(M_{1300}) dM_{1300},$$
 (18)

where $r_{3.5}(M_{1300})$ is the radius up to which the damping wing optical depth is still smaller than 3.5, and the integral is over the luminosity range in which the Ly α transition from the galaxy can survive the damping wing absorption. We use the calibration of Bunker et al. (2004) to convert UV luminosity to star formation rate.

Figure 12 shows the gap length $\Delta r(\tau > 3.5)$ as a function of neutral fraction. In the case of $t_* = 10^7$ yr and $f_e = 0.1$, the average gap length of ~ 80 comoving Mpc at $z \sim 6$ corresponds to a neutral fraction of ~ 0.2 . For a population of star forming galaxies with 10 times more photon production ($\propto f_e t_*$), the same gap length corresponds to $f_{HI} \sim 0.6$, while for a population with 10 times less photons, the constraint on $f_{HI} \sim 0.05$. The constraint in this simple model, however, is only an upper limit on f_{HI} for several reasons: (1) we do not consider the fact that the recombination timescale in the early Universe is long compared to the Hubble time, and assume that all IGM ionization is produced by HII regions around star forming galaxies. In reality, the IGM is probably already largely ionized by previous generations of star forming galaxies; there are highly ionized regions without active star forming galaxies in them at the observed epoch (Wyithe & Loeb 2005); (2) we do not consider the clumpiness of the IGM. Early galaxies are formed in

the highest density, most biased peaks in the density field, and have the highest IGM density in the surrounding region. So the constraint here is closer to the neutral fraction in the densest part of the universe, which is higher than the average neutral fraction; (3) we do not consider the clustering of star forming galaxies at high redshift. If they are strongly clustered, the distance between separate clusters of star forming galaxies is longer for the same IGM neutral fraction. A lower IGM neutral fraction is needed to explain the observed gap length. Therefore, we regard the constraint given in Figure 12 to be an upper limit: the finite distance between dark gaps at $z \sim 6$ suggests that the IGM is not likely to be completely neutral in the regions between HII regions ionized by early star forming galaxies. However, a neutral fraction as high as 10-50% is still permitted in the optimal case.

6. HII Regions Around Quasars

UV photons from a luminous quasar will ionize a HII region (Madau & Rees 2000, Cen & Haiman 2000) in the IGM. The evolution of a cosmological HII region expanding into a neutral IGM is described by the equation (e.g., Shapiro & Giroux 1982, Madau, Haardt & Rees 1999):

$$n_H \left(\frac{dV_I}{dt} - 3HV_I\right) = \dot{N}_Q - \frac{n_H V_I}{t_{\rm rec}},\tag{19}$$

where V_I is the HII region volume, and \dot{N}_Q is the number of ionizing photons the central quasar emits per unit time. When the quasar lifetime is much less than Hubble time, as expected here, the Hubble expansion term is not important. When the HII region is expanding into a partially ionized IGM, as in the case discussed in this paper, (1) the left hand side of Eq. (19) becomes $d(f_{\rm HI}n_HV_I)/dt$, (2) the first term of the right hand side of Eq. (19) becomes $\dot{N}_Q + \epsilon_B V_I$, where ϵ_B is the emissivity of the diffuse UV background. Assuming photoionization-recombination equilibrium in the IGM outside quasar HII region: $\epsilon_B = n_{\rm HII} n_e \alpha(T) = (1 - f_{\rm HI})^2 f_H/t_{\rm rec}$ (for simplicity, we assume a pure hydrogen IGM here), Eq. (19) then changes to:

$$\frac{d(f_{\rm HI}n_H V_I)}{dt} = \dot{N}_Q - \frac{(2 - f_{\rm HI})f_{\rm HI}n_H V_I}{t_{\rm rec}}.$$
 (20)

The quasar ionizing photons are only responsible for ionizing a fraction $f_{\rm HI}$ of the IGM, while the rest is ionized by the diffuse UV background same as the case outside quasar HII region. The factor of $(2 - f_{\rm HI})$ in Eq. (20) arises from the $(1 - f_{\rm HI})^2$ dependence in photoionization-recombination equilibrium equation. In the case of a mostly ionized IGM, $f_{\rm HI} \ll 1$, we have

$$\frac{d(f_{\rm HI}n_H V_I)}{dt} = \dot{N}_Q - \frac{2f_{\rm HI}n_H V_I}{t_{\rm rec}}.$$
 (21)

Therefore, for the same quasar lifetime t, the HII region size scales as

$$R_s \propto \left(\frac{\dot{N}_Q}{2f_{\rm HI}}\right)^{1/3}$$
 (22)

This scaling applies for both the cases in which quasar lifetime is longer or shorter than the recombination time. When recombination is not important (Madau & Rees 2000, Cen & Haiman 2000, cf. Yu & Lu 2005), Cen & Haiman (2002) show that the HII region has a radius

$$R_s = 8.0 f_{HI}^{-1/3} (\dot{N}_Q / 6.5 \times 10^{57} \text{s}^{-1})^{1/3} (t_Q / 2 \times 10^7 \text{yr})^{1/3} [(1 + \text{z}_Q) / 7]^{-1} \text{proper Mpc.}$$
 (23)

This is the same as Eq. (15), now expressing the source luminosity in terms of the photon production rate. The SDSS $z\sim 6$ quasars would produce HII regions with R_s of the order several Mpc if the IGM were largely neutral (e.g., Pentericci et al. 2002, White et al. 2003). A number of authors (Mesinger & Haiman 2004, Wyithe & Loeb 2004a, Wyithe et al. 2005, Yu & Lu 2005) used the observed size of the HII regions around a number of SDSS $z\sim 6$ quasars to constrain the IGM neutral fraction, and suggested that the IGM could have neutral fraction $\gtrsim 0.2$ outside the quasar HII region. Using this size to derive the IGM neutral fraction, however, is complicated by a number of factors:

- 1. Uncertainties in the quasar lifetime. Current observations suggest that quasar lifetimes lie in the range 10^5 10^8 years (e.g. Hopkins et al. 2005, Martini & Weinberg 2001). Most studies have assumed a lifetime of $\sim 10^7$ yrs, similar to the Eddington timescale for black hole growth. For a given R_s , $f_{\rm HI} \sim t_Q$ when recombination is not important.
- 2. Uncertainties in the ionizing photon production rate by the quasar for a given UV luminosity.
- 3. Radiative transfer and clumpiness of the IGM within the quasar HII region, which will affect the *apparent* line of sight size of the HII region.
- 4. Contribution of ionizing photons from galaxies in the overdense environment of luminous quasars.
- 5. Large scale clustering of the IGM around luminous quasars at $z \sim 6$, which are highly biased, will affect the estimates of the IGM neutral fraction.

The last two factors could result in significant overestimation of the neutral fraction. The SDSS quasars considered here are very rare objects (spatial density $\sim 10^{-9}~\rm Mpc^{-3}$) and thus are likely to live in highly biased environment in the early Universe. Fan et al. (2001) estimated that these quasars correspond to 5-6 σ peaks in the density field. Yu & Lu (2005) argued that up to $\sim 90\%$ of the neutral hydrogen could have already been ionized by the star forming galaxies associated with this high density peak. Mesinger & Haiman (2004) showed that by comparing high S/N, high resolution spectra with detailed hydrodynamic simulations of quasar HII regions, it is possible to reliably estimate the neutral fraction and minimize the degeneracies with quasar lifetime and bolometric luminosity along some lines of sight.

For these reasons, the *absolute measurement* of the neutral fraction based on HII region size could be off by a large factor. Over the narrow redshift range considered here, these systematics

are likely to be roughly the same on average for all the quasars. If there is an order of magnitude evolution in the IGM ionization, the size of the HII region should show strong evolution, providing a reliable *relative* measurement of neutral fraction. In this section, we study the distribution and evolution of HII region sizes around the nineteen $z \sim 6$ quasars in our sample.

We first examine the definition and measurement of the HII region size around quasars. The physical picture is that quasars are located within an IGM with neutral fraction $f_{\rm HI}$. As the quasar evolves, its ionizing flux produces a surrounding region within which the IGM is completely ionized. We have shown above that for a partially ionized IGM, the size of this proximity zone grows as $\sim \dot{N}_Q^{1/3} t_Q^{1/3}$. In the case that the recombination timescale is long, this is not a picture of a static Strömgren sphere. When the general IGM is already highly ionized (valid at least up to $z \sim 6$, as we have seen), it is not even a standard HII region. It is also very different from the classic foreground proximity effect at lower redshift (e.g. Bajtlik, Duncan, & Ostriker 1988, Scott et al. 2002). At z < 5, the IGM ionizing background is much higher. At a distance R_s from the quasar, the UV background itself is much larger than the flux intensity produced by the quasar in question. Furthermore, the mean free path of ionizing photons is much larger than R_s calculated above. In this case, the expanding proximity zone does not have a clear boundary. The proximity effect is simply an excess of ionizing background and increased ionization close to the quasar.

At $z \sim 6$, with a low UV background, the quasar flux does produce a highly ionized proximity zone with a well-defined boundary expanding into the general IGM. However, the boundary of this proximity zone can be difficult to measure observationally. It cannot be simply defined as the point at which the transmitted flux reaches zero for the following reasons: (a) if the IGM is highly ionized, not only does the transmission never reach zero on average, it has also large fluctuations (§3). Simply defining the size of the proximity zone as the point at which the flux reaches zero will overestimate its size at low redshift. (b) The IGM transmission is characterized by a mixture of dark gaps and sharp transmission peaks (§5). Using zero flux as the boundary is affected by the resolution and smoothing length used. (c) In the case of a neutral IGM, reaching zero flux does not necessarily mean reaching the boundary of the proximity zone: the IGM could still be ionized by the quasar to a level much higher than the surrounding material, but with optical depth higher than the detection limit $(f_{HI} > 10^{-3})$.

Therefore, instead of using the Strömgren sphere radius R_s , we define the size of the proximity zone R_p as the region where the transmitted flux ratio is above 0.1, when smoothed to a resolution of 20Å. For the quasars in our sample (z > 5.7), the average IGM transmission is smaller than 0.04. Therefore the proximity zone defined this way is not affected by the IGM properties outside the quasar HII region, even with the large observed fluctuation in the IGM transmission. To first order, at R_p , the IGM ionization state is the same for all the quasars, so we have: $R_p \propto (\dot{N}_Q t_Q)^{1/3} (f_{\rm HI})^{-1/3}$. The quasars in our sample have very similar intrinsic properties. So even though we cannot calibrate this relation on an absolute scale, we can use the evolution of R_p to measure the relative change in the IGM neutral fraction into which the quasar HII region is expanding.

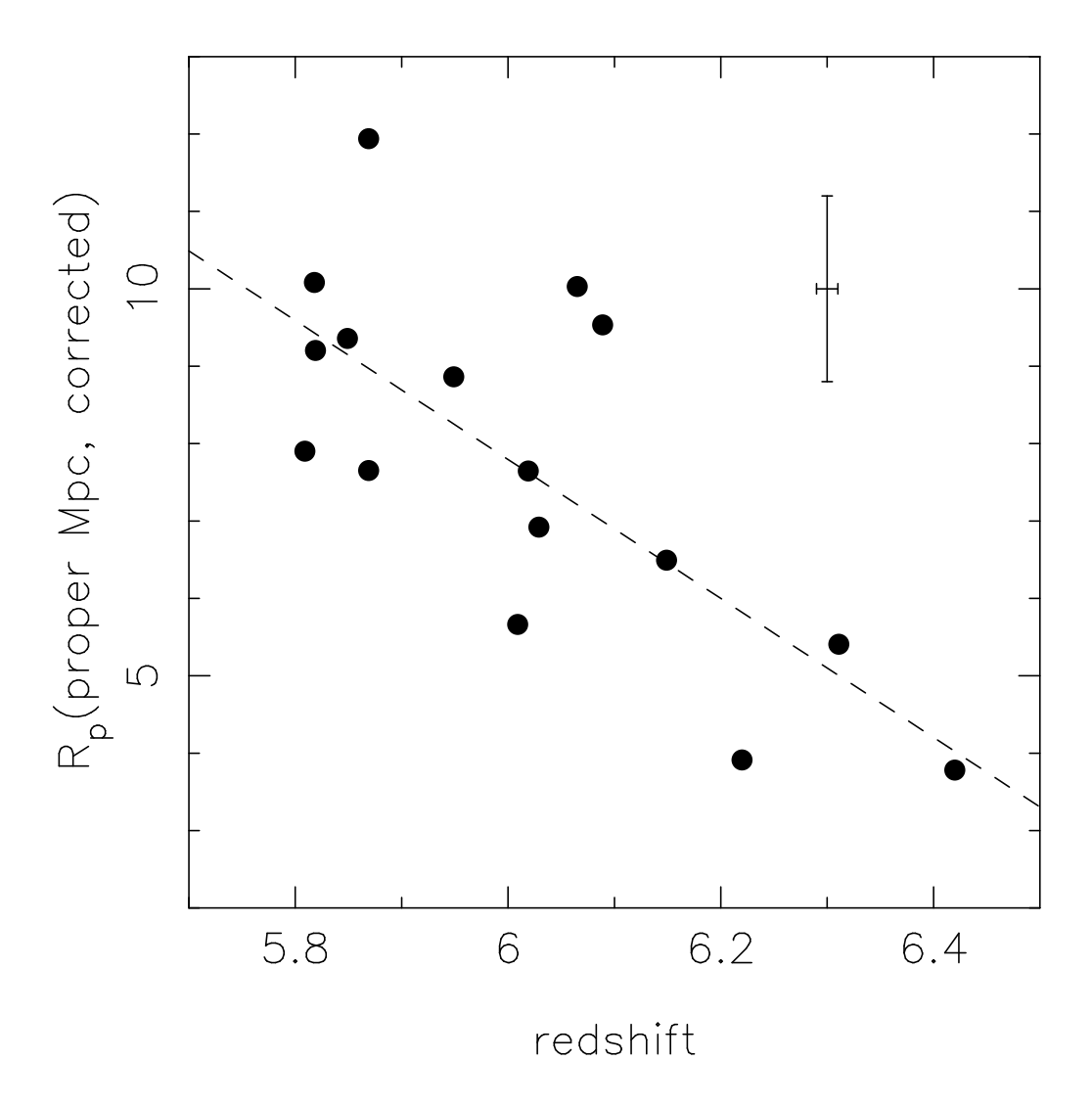


Fig. 13.— Size of quasar proximity zone as a function of the redshift of the quasar. The size R_p is the line of sight distance from the quasar to the point at which the transmitted flux ratio falls to 0.1 of the continuum level. The radius also has been scaled to a common absolute magnitude $(M_{1450} = -27)$. The linear fit shows a factor of 2.8 decrease in the HII region size around quasars from z = 5.7 to 6.4. The error on R_p is dominated by the uncertainty in the quasar redshift.

The other uncertainty comes from the difficulty in determining the quasar redshift. It is well known that there is a systematic velocity offset between high-ionization emission lines such as CIV and SiIV and the systematic redshift of the quasar host galaxy, as measured by narrow lines such as [OIII], or CO molecular lines in the host galaxy. On the other hand, low-ionization lines such as MgII show little offset from the systematic redshift. Richards et al. (2002b) used a large sample of SDSS quasars to show that CIV is blueshifted from MgII by 824 ± 511 km s⁻¹. At $z \sim 6$, we have $z_{\rm MgII} = z_{\rm CIV} + (0.019 \pm 0.012)$. Most of the redshifts in Table 1 are determined using high-ionization lines such as CIV, SiIV or NV. When calculating the size of the proximity zone, this shift becomes a major source of systematic error. Five of the quasars in our sample have MgII or CO redshifts: J1148+5251: $z_{\rm CO} = 6.42$ (Walter et al. 2003), J1623+3112: $z_{\rm MgII} = 6.22$ (L. Jiang et al. in preparation), J1630+4012: $z_{\rm MgII} = 6.07$, J1030+0524: $z_{\rm MgII} = 6.31$ (Iwamuro et al. 2004), and J0836+0054: $z_{\rm MgII} = 5.82$ (Pentericci et al. 2005). We adopt the MgII or CO redshift for these five objects when calculating the size of the proximity zone. For the rest of the sample, we assume $z_{\rm MgII} = z_{\rm high-ionization} + 0.02$ in the calculation, and an uncertainty in the redshift determination of 0.02.

Figure 13 shows R_p as a function of redshift. We have scaled R_p to a common absolute magnitude $M_{1450} = -27$ (assumed to be proportional to \dot{N}_q) as R_p (corrected) $= R_p \times 10^{-0.4(-27+M_{1450})/3}$. Correcting for luminosity differences significantly tightens the scatter around a linear regression. We also exclude the two BAL quasars as well as SDSS J1335+3533 (z = 5.94) from this test. The latter object is a lineless quasar presented in Fan et al. (2005), in which we used the size of the proximity zone to estimate its redshift. The error bars on R_p are dominated by the uncertainties in the emission line redshift of the quasars $\sigma(z_{em}) \sim 0.02$, yielding an uncertainty of ~ 1.2 Mpc. The solid line in Figure 13 is the best linear fit of R_p as a function of redshift:

$$R_p = 6.7 - 8.1 \times (z - 6) \text{ Mpc.}$$
 (24)

This linear relation has a Pearson correlation coefficient of 0.72, which is significant at the 99.8% level for our sample of 16 quasars. We use this linear fit only to establish the correlation between R_p and redshift, rather than making any detailed statement about the functional dependence of R_p on z. From z = 5.7 to 6.4, the average size of the proximity zone R_p has decreased from 9.1 Mpc to 3.5 Mpc, a factor of 2.8. From Figure 13, the scatter of HII region sizes at any given redshift is of the order of 2 Mpc, not significantly larger than the size of the error bar. Based on Eq. (23), this indicates a small dispersion in intrinsic quasar properties, such as bolometric correction, quasar lifetime and relative bias of the quasar environment, at a given redshift.

Figure 14 shows the mean absorption profiles in the quasar proximity zones as a function of redshift. We do not scale the profile according to quasar luminosity in this case. The profile is noisy due to the small number of quasars (4–8) in different redshift bins and the presence of strong absorption lines within the proximity zones, due to the clumpy IGM close to the quasar. However, the evolutionary trend is evident: the z=5.7-5.9 profile is the most extended; the transmission declines to ~ 0.1 at $\sim 8-10$ Mpc. The z=5.9-6.1 profile reaches the same level at $R_p \sim 7$ Mpc,

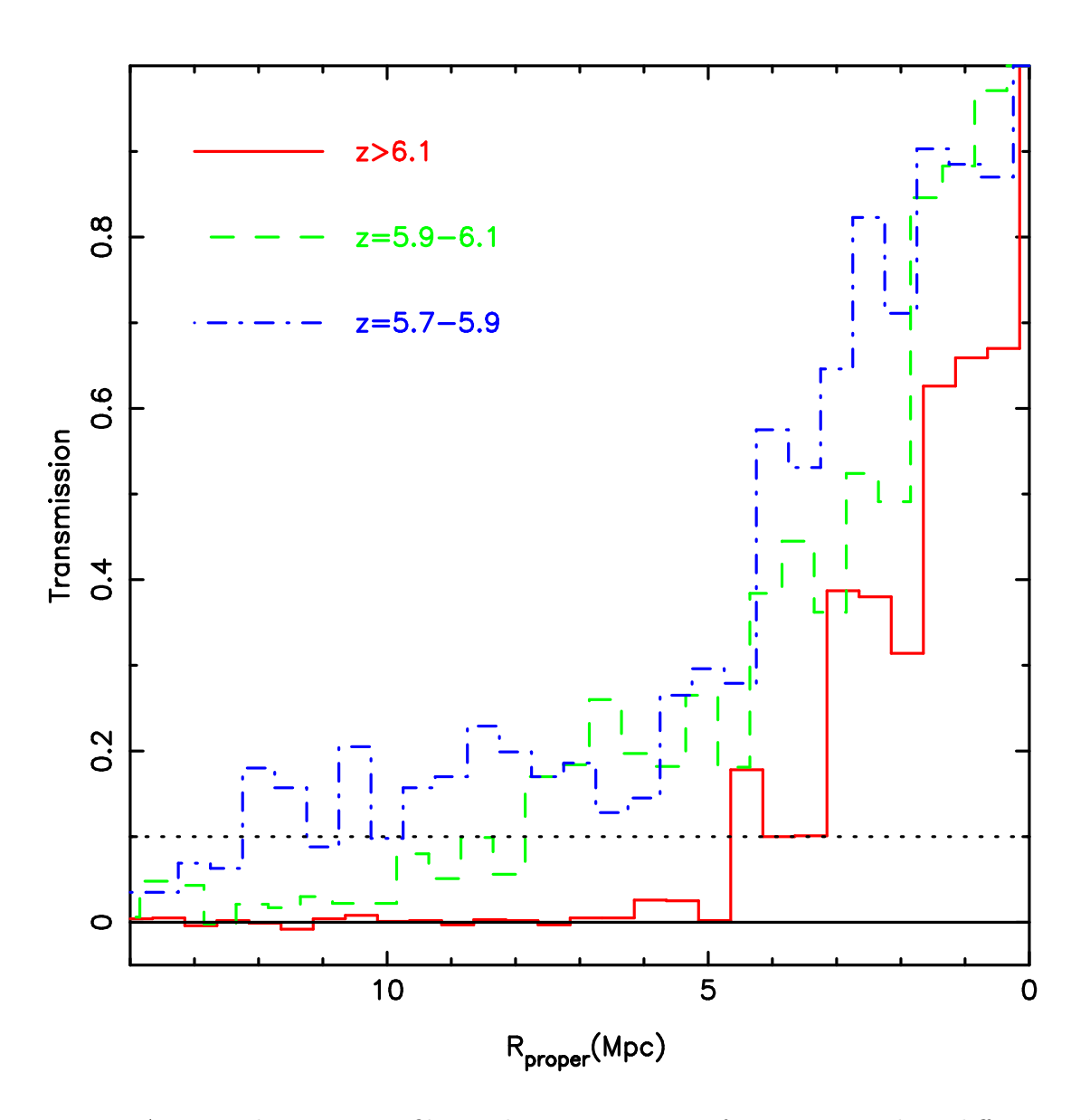


Fig. 14.— Average absorption profiles in the proximity zone for quasars at three different redshift bins: z=5.7-5.9, z=5.9-6.1 and z>6.1. The Ly α +NV emission profile has been fitted with a Gaussian and removed. The absorption profile is significantly narrower at z>6.1 than at lower redshifts.

while the profile at z > 6.1 is the narrowest, declining to $\mathcal{T} = 0.1$ after only ~ 3 Mpc. This trend is not significantly affected by the choice of binning. Also note that the profiles in the low redshift bins continue to decline beyond R_p until reaching the IGM level, but the level never reaches zero flux. Only in the highest redshift bin does the profile reach zero flux, as the IGM outside the quasar HII region has $\tau \gtrsim 5$. For z > 6, when the flux outside the HII region does reach zero, the proximity zone size R_p defined this way is $\sim 20\%$ smaller than that using the zero-flux size.

The significant evolution of the size of quasar HII regions validates the physical picture that quasar HII regions are expanding into an increasingly neutral IGM at higher redshift. Since $R_p \propto [(1+z)f_{\rm HI}]^{-1/3}$ (after scaling out the dependence on quasar luminosity), a decrease of HII region sizes by a factor of 2.8 from z=5.7 to 6.4 suggests an increase of the neutral fraction by a factor of 14. Note that this relation applies when $f_{\rm HI} \ll 1$, as in the case here; at larger nuetral fraction, a detailed solution of Eq. (20) is required. This constraint on the relative increase of the neutral fraction does not depend on the model of photoionization and IGM density distribution we used in §3.

Mesinger & Haiman (2004) examined the absorption profile in the line of sight of SDSS J1030+0534 (z=6.28). In this line of sight, the Ly β transition reaches zero flux at a redshift ~ 0.02 lower than that of the Ly α transition. They model this feature as the boundary of a Strömgren sphere, and suggest that the size of this Strömgren sphere is consistent with a largely neutral IGM. From Figure 10, we clearly see the extra transmission in Ly β for SDSS J1030+0524. However, we do not observe this feature in any other line of sight.

Our GP optical depth measurements show that at $z_{abs} \sim 5.7$, the volume- and mass-averaged neutral fractions are $\sim 9.3 \times 10^{-5}$ and 2.8×10^{-3} respectively (see Figure 7). Our result here implies that the neutral fraction has increased by a factor of 14 at $z \sim 6.4$, to 1.3×10^{-3} and 0.04, respectively. Note that the high mass averaged neutral fraction of 0.04 is lower than several previous estimates (Mesinger & Haiman 2004, Wyithe et al. 2005) based on measurements of HII region size, but still is in general agreement. Our estimate of neutral fraction evolution is based on a simple model in which a uniform UV background ionizes the IGM to a neutral fraction of $f_{\rm HI}$, and the quasar provides the extra UV photons that produce a completely ionized HII region. Yu & Lu (2005) describe a more detailed, self-consistent model that includes ionization from both stellar sources and quasars. Their model considers in detail the influence of the bias factor of quasar environment and quasar lifetime on the size of the quasar HII region. Such detailed modeling is beyond the scope of this paper.

7. Discussion and Summary

The goal of this paper is to study the evolution of the IGM ionization state near the end of reionization using absorption spectra of the highest redshift quasars known. We use three types of measurements to study IGM properties. We now discuss their advantages and disadvantages,

with an eye towards application to yet higher redshift.

- 1. Evolution of Gunn-Peterson optical depth. In §3, we measured the GP optical depth in the Ly α , Ly β and Ly γ transitions. This is directly linked to the neutral hydrogen density of the IGM. Using a photoionization model, we can compute the underlying UV ionizing background, and estimate the neutral fraction and mean free path of UV photons. However, as the optical depth increases to $\tau \gtrsim 5$ at z > 6, the Ly α transition becomes completely saturated. It is difficult to place stronger constraints as the measurement begins to be dominated by systematic observational errors in the red and near-IR part of the spectrum. The Ly β and Ly γ transitions (§3.2) give more stringent constraints due to their smaller oscillator strengths, but they can only improve the limit by a factor of 2-4. In addition, one has to correct for the foreground absorption from lower order transitions. Direct measurement of the GP optical depth can only constrain the neutral fraction of the IGM to lower limits in the range $\sim 10^{-3}$ to 10^{-2} . Since at high redshift, all IGM transmission is through a small number of transmitting spikes with high ionization and/or low density, the effective optical depth is actually not sensitive to the region of the IGM where most of the neutral hydrogen lies. Furthermore, the interpretation of optical depth depends on the photoionization model and IGM density distribution models used. The exact values of derived ionization parameters, such as ionizing background and neutral fraction. are therefore model-dependent. But for a narrow redshift range, our calculation shows a robust strong evolutionary trend on the ionization parameters. Thus using the evolution of GP optical depth is most useful at the low redshift end, and it begins to lose its usefulness when the neutral fraction increases to $\sim 10^{-3}$.
- 2. Distribution of Gunn-Peterson troughs and dark gaps. In §4, we discussed using the distribution of absorption gaps to characterize the evolution of the IGM. Qualitatively, these statistics reveal very similar trends to the GP optical depth measurements. But they also contain high order information, related to the clustering of transmission spikes and dark gaps. The evolution of dark gaps appears to be the most sensitive quantity tracing the reionization process: of the statistics we examine, it shows the most dramatic evolution at z > 6. The distribution of dark gap length is readily computable from both observations and cosmological simulations. Simulations show that even when the average neutral fraction is high, the dark gap length is still finite due to the presence of regions that were ionized by star-forming galaxies. In §5.3, we used the length of dark gaps and the observed galaxy luminosity function at $z \sim 6$ to put an independent upper limit on the IGM neutral fraction. Of course, these statistics are not straightforward to calculate from analytic or semi-analytic models, and must be derived from detailed simulations that include the clustering of the IGM and ionizing sources, and take into account spectral resolution and S/N of observed spectra.
- **3.** HII regions around high-redshift sources. In §6, we measured the HII region sizes around high-redshift quasars, and showed that the sizes decrease significantly with redshift, consistent with a rapid increase in the IGM neutral fraction. This method provides a powerful and independent way of measuring the IGM neutral fraction, and can in principle be applied to regions with high

neutral fraction if luminous sources can be discovered. The disadvantage is that the sizes of HII regions are quite model dependent: theoretical calculations require not only knowledge of IGM properties, but also the intrinsic properties of quasars, including their lifetime and bias relative to the density field at high redshift. Further theoretical modelling will improve this constraint. As these quantities are unlikely to change over the redshift range we probe, we used the HII region sizes as a robust measure of the *fractional* change in the neutral fraction over this redshift range.

In §1, we posed three questions regarding the evolution of the IGM and the end of reionization. We now present our major conclusions based on our analysis of this sample of nineteen z > 5.7 quasars.

- 1. There is a strong evolution of the IGM ionization state at high redshift, in terms of the effective GP optical depth, the derived UV background, the neutral fraction, the mean free path of UV photons, and the extent of dark gaps. This evolution accelerates at z > 5.7. The GP optical depth evolution changes from $\tau_{\rm GP}^{\rm eff} \sim (1+z)^{4.3}$ to $(1+z)^{\gtrsim 11}$, indicating a lower limit in the increase in the volume-averaged neutral fraction of a factor of 7 between z = 5.5 and 6.2.
- 2. Accompanying the increased average neutrality of the IGM is a rapid increase in the relative dispersion of IGM properties along different lines of sight. We find that this increased dispersion implies fluctuations by a factor of $\gtrsim 4$ in the UV background at z>6. This is not surprising, as the mean free path of UV photons at $z\sim 6$ is comparable to the correlation length of star forming galaxies which likely provide most of the photons that ionized the Universe.
- 3. The most effective measure of the IGM evolution at high redshift is the distribution of dark absorption gaps in the IGM. The average length of dark gaps shows a dramatic increase at $z \sim 6$. This quantity shows the largest line of sight variations: dark gaps as long as 50 comoving Mpc appear by $z \sim 5.5$, while some lines of sight at z > 6 are still somewhat transparent.
- 4. Using the evolution of HII region sizes around the quasars, we find the neutral fraction of the IGM has increased by ~ 14 between z=5.5 and 6.4, consistent with our GP optical depth estimates. This implies a mass-averaged neutral fraction as high as $\sim 4\%$ in regions around luminous quasars at $z\sim 6.4$.
- 5. There is no compelling evidence that the IGM at $z \sim 6.4$ is largely neutral. On the contrary, the finite length of dark gaps in the spectra implies an upper limit on the neutral fraction less than 50%, likely even lower.

Figure 15 summarizes our constraints on the mass-averaged neutral fraction using quasar spectra presented in this paper. The analysis here confirms the main result of Paper I based on

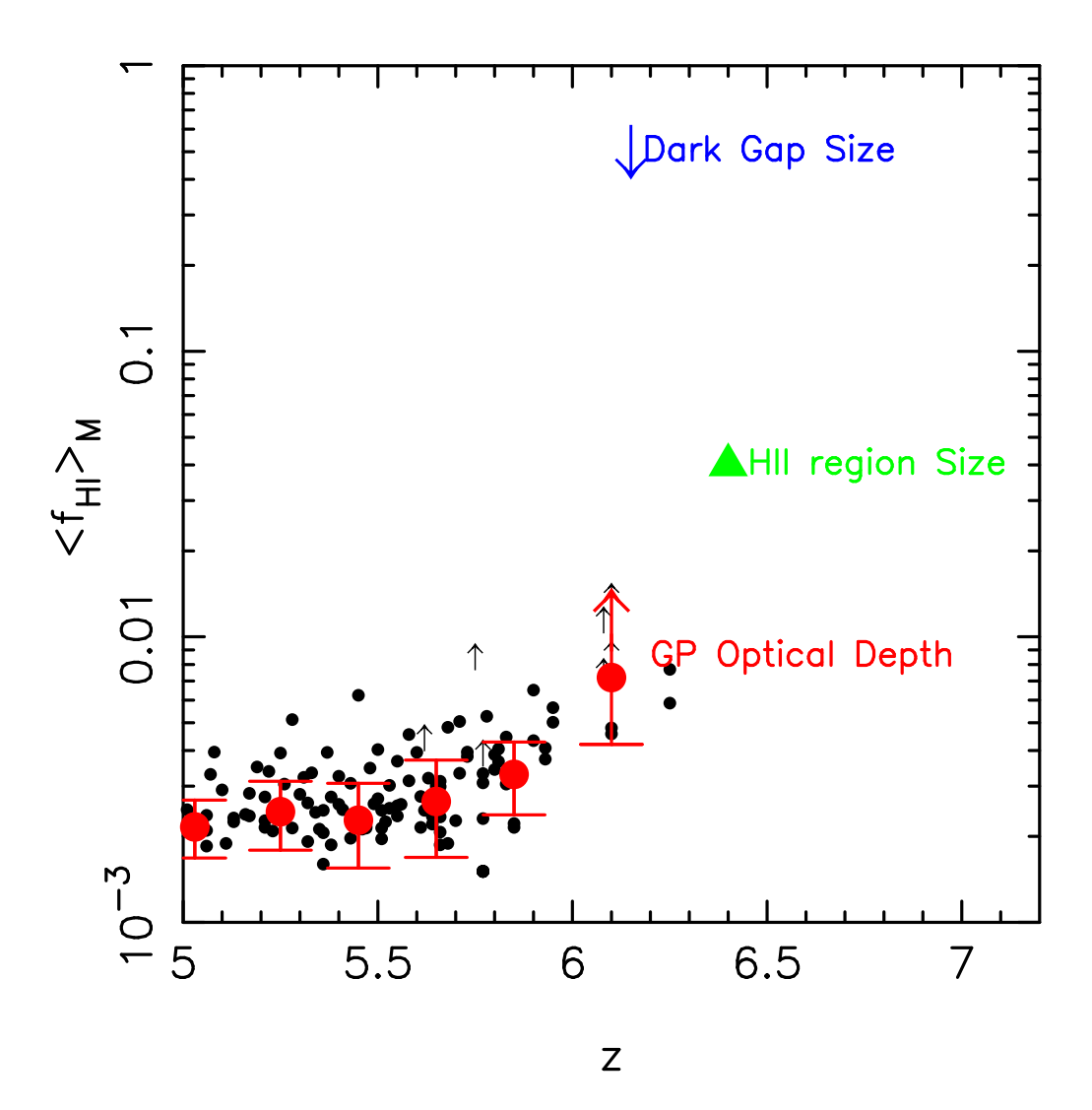


Fig. 15.— The evolution of the mass-averaged neutral fraction using constraints from GP optical depth measurements, HII region size evolution, and distribution of dark absorption gaps.

only four quasars: the detections of deep GP troughs indicate an accelerated rate of IGM evolution at z > 5.7, consistent with the IGM transition at the end of the overlapping stage of reionization. However, the results do not indicate that the IGM has achieved a high level of neutrality at $z \sim 6$. The large dispersion of the IGM properties along different lines of sight strongly suggests that the reionization process is complex and not likely a uniform phase transition over a very narrow redshift range.

If luminous sources at $z \sim 6-10$ can be discovered by JWST and next generation wide-field IR surveys, statistics of dark gaps in their absorption spectra and measurements of HII region sizes surrounding these sources will provide the most useful probe of the history of reionization using high-redshift discrete sources, and complement constraints from CMB polarization measurements (e.g. PLANCK) and 21cm experiments (e.g. LOFAR, MWA, PAST and SKA).

Funding for the Sloan Digital Sky Survey (SDSS) has been provided by the Alfred P. Sloan Foundation, the Participating Institutions, the National Aeronautics and Space Administration, the National Science Foundation, the U.S. Department of Energy, the Japanese Monbukagakusho. the Max Planck Society, and the HEFCE. The SDSS is a joint project of The University of Chicago, Fermilab, the Institute for Advanced Study, the Japan Participation Group, The Johns Hopkins University, the Korean Scientist Group, Los Alamos National Laboratory, the Max-Planck-Institute for Astronomy (MPIA), the Max-Planck-Institute for Astrophysics (MPA), New Mexico State University, University of Pittsburgh, University of Portsmouth, Princeton University, the United States Naval Observatory, and the University of Washington. We thank Andrea Ferrara, Doug Finkbeiner, Steve Furlanetto, Nick Gnedin, Zoltan Haiman, Avery Meiksin. Mike Norman, Peng Oh, Stuart Wyithe, and Idit Zehavi for helpful discussions, and the referee for valuable comments and suggestions. XF thanks KITP for hospitality during part of this project. We acknowledge support from NSF grant AST 03-07384, a Sloan Research Fellowship, a Packard Fellowship for Science and Engineering (X.F.), NSF grant AST 03-07409 (M.A.S.,) the Institute of Geophysics and Planetary Physics (operated under the auspices of the US Department of Energy by Lawerence Livermore National Laboratory under contract No. W-7045-Eng-48) (R. H. B.) and NSF grant AST 03-07582 (D.P.S.).

REFERENCES

Abazajian, K., et al. 2003, AJ, 126, 2081

Abazajian, K., et al. 2004, AJ, 129, 1755

Abel, T., Anninos, P., Zhang, Y., & Norman, M. L., 1997, NewA, 2, 181

Adelberger, K. L., Steidel, C. C., Pettini, M., Shapley, A. E., Reddy, N. A., & Erb, D. K. 2005, ApJ, 619, 697

Adelman-McCarthy, J., et al. 2006, ApJS, 162, 38

Arav, N., et al. 2001, ApJ, 561, 118

Bajtlik, S., Duncan, R.C., & Ostriker, J.P. 1988, ApJ, 327, 570

Barkana, R. 2003, New Astronomy, 7, 337

Barkana, R., & Loeb, A., 2001, Physics Reports, 349, 125

Becker, G. D., Sargent, W. L., Rauch, M., & Simcoe, R. A. 2006, ApJ, submitted (astro-ph/0511541)

Becker, R. H. et al. 2001, AJ, 122, 2850

Benson, A. J., Nusser, A., Sugiyama, N., & Lacey, C. G. 2001, MNRAS, 320, 153

Bouwens, R. J., et al. 2004a, ApJ, 606, L25

Bouwens, R. J., et al. 2004b, ApJ, 616, L79

Bunker, A. J., Stanway, E. R., Ellis, R. S., & McMahon, R. G. 2004, MNRAS, 355, 374

Cen, R. 2003a, ApJ, 591, 12

Cen, R. 2003b, ApJ, 591, L5

Cen, R. 2003c, ApJ, 597, L13

Cen, R., Miralda-Escudé, J., Ostriker, J. P., & Rauch, M., 1994, ApJ, 437, L9

Cen, R., & Haiman, Z., 2000, ApJ, 542, L75

Cen, R. & McDonald, P. 2002, ApJ, 570, 457

Chiu, W. A., Fan, X., & Ostriker, J. P. 2003, ApJ, 599. 759

Chiu, W. A., & Ostriker, J. P., 2000, ApJ, 534, 507

Choudhury, T. R., & Ferrara, A. 2005, MNRAS, 361, 577

Ciardi, B., Ferrara, A., Marri, S., & Raimondo, G., 2001, MNRAS, 324, 381

Ciardi, B, Ferrara, A., & White, S. D. M. 2003, MNRAS, 344, L7

Ciardi, B & Ferrara, A. 2005, Space Science Review, 116, 625

Croft, R. A. C. 1998, Eighteenth Texas Symposium on Relativistic Astrophysics, 664

Dijkstra, M., Haiman, Z., & Loeb, A. 2004, ApJ, 613, 646

Djorgovski, S. G., Castro, S., Stern, D., & Mahabal, A. A. 2001, ApJ, 560, L5

Epps, H.W., & Miller, J.S. 1998, Proc. SPIE, 3355, 48

Fan, X. et al., 2000, AJ, 120, 1167

—, 2001, AJ, 122, 2833

—, 2002, AJ, 123, 1247 (Paper I)

—, 2003, AJ, 125, 1649

—— 2004, AJ, 128, 515

— 2006, AJ, 131, 1203

Fukugita, M., Ichikawa, T., Gunn, J.E., Doi, M., Shimasaku, K., & Schneider, D.P. 1996, AJ, 111, 1748

Furlanetto, S., Hernquist, L., & Zaldarriaga, M. 2004, MNRAS, 354, 675

Furlanetto, S., Zaldarriaga, M., & Hernquist, L. 2006, MNRAS, 365, 1012

Furlanetto, S., & Oh, S. P. 2005, MNRAS, 363, 1031

Gnedin, N., 2000, ApJ, 535, 530

Gnedin, N. Y. 2004, ApJ, 610, 9

Goodrich, R. W., et al. 2001, ApJ, 561, L23

Gunn, J. E., & Peterson, B. A. 1965, ApJ, 142, 1633

Gunn, J.E., et al. 1998, AJ, 116, 3040

Gunn, J.E., et al. 2006, AJ, in press (astro-ph/0602326)

Haiman, Z. 2002, ApJ, 576, L1

Haiman, Z. & Holder, G. P. 2003, ApJ, 595, 1

Haiman, Z., & Cen, R. 2005, ApJ, 623, 627

Hogg, D., et al. 2001, AJ, 122, 2129

Hopkins, P. F., Hernquist, L., Martini, P., Cox, T. J., Robertson, B., Di Matteo, T., & Springel, V. 2005, ApJ, 625, L71

Hu, E. M., Cowie, L. L., Capak, P., McMahon, R. G., Hayashino, T., & Komiyama, Y. 2004, AJ, 127, 563

Hu, E. M., Cowie, L. L., Capak, P., Kakazu, Y. 2005, to appear in IAU 199 Conf. Proc.: "Probing Galaxies through Quasar Absorption Lines," eds. Williams, Shu, Menard (astro-ph/0509616)

Hui, L. & Haiman, Z. 2003, ApJ, 596, 9

Ivezić, Ž., et al. 2004, Astronomische Nachrichten, 325, 583

Iwamuro, F., Kimura, M., Eto, S., Maihara, T., Motohara, K., Yoshii, Y., & Doi, M. 2004, ApJ, 614, 69

Kaiser, N., & Peacock, J. A. 1991, ApJ, 379, 482

Kashikawa, N. et al. 2006, ApJ, 637, 631

Kogut, A. et al. 2003, ApJS, 148, 161

Kohler, K., Gnedin, N. Y., & Hamilton, A. J. S. 2005, astro-ph/0511627

Lidz, A., Hui, L., Zaldarriaga, M., & Scoccimarro, R. 2002, ApJ, 579, 491

Loeb, A., & Barkana, R., 2001, ARA&A, 39, 19

Lupton, R.H., Gunn, J.E., & Szalay, A. 1999, AJ, 118, 1406

Lupton, R. H., Gunn, J. E., Ivezic, Z., Knapp, G. R., Kent, S. M., & Yasuda, N., 2001, ASP Conf. Ser. 238: Astronomical Data Analysis Software and Systems X, 269

Madau, P., Haardt, F., & Rees, M. J. 1999, ApJ, 514, 648

Madau, P., & Rees, M. J. 2000, ApJ, 542, L69

Mahabal, A., Stern, D., Bogosavljevic, M., Djorgovski, S. G., & Thompson, D. 2005, ApJ, 634, L9

Maiolino, R., Schneider, R., Oliva, E., Bianchi, S., Ferrara, A., Mannucci, F., Pedani, M., & Roca Sogorb, M. 2004, Nature, 431, 533

Malhotra, S., et al. 2005, ApJ, 626, 666

Malhotra, S., & Rhoads, J. E. 2004, ApJ, 617, L5

Malhotra, S., & Rhoads, J. E. 2006, ApJL, submitted (astro-ph/0511414)

Martini, P., & Weinberg, D. H. 2001, ApJ, 547, 12

McDonald, P., & Miralda-Escudé, J., 2001, ApJ, 549, L11

McDonald, P., et al. 2005, ApJ, 635, 761

Meiksin, A. 2005, MNRAS, 356, 596

Melchiorri, A., Choudhury, T. R., Serra, P., & Ferrara, A. 2005, MNRAS, 364, 873

Mesinger, A., & Haiman, Z. 2004, ApJ, 611, L69

Mesinger, A., Haiman, Z., & Cen, R. 2004, ApJ, 613, 23

Miralda-Escudé, J., Cen, R., Ostriker, J. P., & Rauch, M., 1996, ApJ, 471, 582

Miralda-Escudé, J., 1998, ApJ, 501, 15

Miralda-Escudé, J., Haehnelt, M., & Rees, M. J., 2000, ApJ, 530, 1

Oh, S. P., & Furlanetto, S. R. 2005, ApJ, 620, L9

Paschos, P., & Norman, M. L., 2005, ApJ, 631, 59

Pentericci, L., et al. 2002, AJ, 123, 2151

Pentericci, L., et al. 2005, A&A, submitted

Pier, J. et al. 2003, AJ, 125, 1559

Razoumov, A. O., Norman, M. L., Abel, T., & Scott, D., 2002, ApJ, 572, 695

Rees, M. 1999, in After the Dark Ages: When Galaxies were Young (the Universe at 2 < z < 5), ed. S. S. Holt and E. P. Smith, (AIP Press), 13

Reichard, T. A., et al. 2003, AJ, 126, 2594

Richards, G. T., et al. 2002a, AJ, 123, 2945

Richards, G. T., Vanden Berk, D. E., Reichard, T. A., Hall, P. B., Schneider, D. P., SubbaRao, M., Thakar, A. R., & York, D. G. 2002b, AJ, 124, 1

Santos, M. R. 2004, MNRAS, 349, 1137

Scott, J., Bechtold, J., Morita, M., Dobrzycki, A., & Kulkarni, V. P. 2002, ApJ, 571, 665

Shapiro, P. R., & Giroux, M. L., 1987, ApJ, 321, L107

Smith, J., et al. 2002, AJ, 123, 2121

Somerville, R. S., & Livio, M. 2003, ApJ, 593, 611

Somerville, R. S., Bullock, J. S., & Livio, M. 2003, ApJ, 593, 616

Songaila, A. & Cowie, L. 2002, AJ, 123, 2183

Songaila, A., 2004, AJ, 127, 2598

Spergel, D. N. et al. 2003, ApJS, 148, 175

bibitem[Spergel et al. 2006]Spergel06 Spergel, D. N. et al. 2006, ApJS, submitted

Steidel, C. C., Pettini, M., & Adelberger, K. L. 2001, ApJ, 546, 665

Stern, D., Yost, S. A., Eckart, M. E., Harrison, F. A., Helfand, D. J., Djorgovski, S. G., Malhotra, S., & Rhoads, J. E. 2005, ApJ, 619, 12

Stiavelli, M., Fall, S. M., & Panagia, N. 2004, ApJ, 610, L1

Stoughton, C. et al. 2002, AJ, 123, 485

Tegmark, M., et al. 2004, Phys. Rev. D. 69, 1035 01

Tucker, D., et al. 2006, PASP, submitted

Vanden Berk, D. E., et al. 2001, AJ, 122, 549

Walter, F., et al. 2003, Nature, 424, 406

Weinberg, D. H., Miralda-Escudé, J., Hernquist, L., & Katz, N., 1997, ApJ, 490, 564

White, R. L., Becker, R. H., Fan, X., & Strauss, M. A. 2003, AJ, 126, 1

White, R. L., Becker, R. H., Fan, X., & Strauss, M. A. 2005, AJ, 129, 2102

Wyithe, J. S. B., & Loeb, A. 2003a, ApJ, 586, 693

Wyithe, J. S. B., & Loeb, A. 2003b, ApJ, 588, L69

Wyithe, J. S. B., & Loeb, A. 2004a, Nature, 427, 815

Wyithe, J. S. B., & Loeb, A. 2004b, Nature, 432, 194

Wyithe, J, S. B., & Loeb, A. 2005, ApJ, 625, 1

Wyithe, J. S. B., Loeb, A., & Carilli, C. 2005, ApJ, 628, 575

Yan, H., Windhorst, R. A., Odewahn, S. C., Cohen, S. H., Röttgering, H. J. A., & Keel, W. C. 2002, ApJ, 580, 725

Yan, H., & Windhorst, R. A. 2004a, ApJ, 600, L1

Yan, H., & Windhorst, R. A. 2004b, ApJ, 612, L93

York, D. G., et al. 2000, AJ, 120, 1579

Yu, Q., & Lu, Y. 2005, ApJ, 620, 31

Yu, Q. 2005, ApJ, 623, 683

Zehavi, I., et al. 2005, ApJ, 630, $\boldsymbol{1}$

This preprint was prepared with the AAS IATEX macros v4.0.

Table 1. Spectroscopic Observations of the $z\sim 6$ Quasar Sample

Quasar (SDSS)	redshift	M_{1450}	Telescope ¹	Exposure (hours)	Ref^2
J114816.64+525150.3	6.42	-27.8	Keck	11.5	4,5
J103027.10 + 052455.0	6.28	-27.2	Keck	10.3	2,5
J162331.81 + 311200.5	6.22	-26.6	Keck	1.0	6,8
$J104845.05 + 463718.3^3$	6.20	-27.6	Keck	4.5	4,8
J125051.93 + 313021.9	6.13	-27.1	Keck	1.0	7,7
$J160253.98 + 422824.9^4$	6.07	-26.8	MMT	1.3	6,6
J163033.90 + 401209.6	6.05	-26.1	HET	1.0	$4,\!4$
J113717.73 + 354956.9	6.01	-27.1	Keck	0.7	7,7
J081827.40 + 172251.8	6.00	-27.4	Keck	0.3	7,7
J130608.26 + 035626.3	5.99	-26.9	Keck	0.2	2,3
J133550.81 + 353315.8	5.95	-26.8	MMT	2.0	7,7
J141111.29 + 121737.4	5.93	-26.8	Keck	1.0	6,8
J084035.09 + 562419.9	5.85	-26.6	MMT	1.0	7,7
J000552.34 - 000655.8	5.85	-26.5	Keck	0.3	6,8
J143611.74 + 500706.9	5.83	-26.3	MMT	1.0	7,7
J083643.85 + 005453.3	5.82	-27.8	Keck	0.3	2,3
J000239.39 + 255034.8	5.80	-27.7	MMT	1.0	6,6
J092721.82 + 200123.7	5.79	-26.8	KP	3.7	7,7
$\rm J104433.04\!-\!012502.2^3$	5.74	-27.5	Keck	0.7	1,1

^{1.} Telescopes and instrument: Keck: Keck/ESI; MMT: MMT/Red Channel; KP: Kitt Peak 4-meter/MARS

^{2.} References of discovery spectrum and spectrum presented here; (1). Fan et al. 2000, (2). Fan et al. 2001, (3) Becker et al. 2001, (4). Fan et al. 2003, (5). White et al. 2003, (6). Fan et al. 2004, (7). Fan et al. 2005, (8). This paper

^{3.} BAL quasar

^{4.} This object was listed as J160254.18+422822.9 in Fan et al. (2004); the position given here reflects improved astrometry.

Table 2. $\,$ Ly $\!\alpha$ Transmitted Flux Ratio

Quasar	z_{em}	z_{abs}	T
J0002+2550	5.80	5.58	0.0170 ± 0.0062
		5.43	0.0573 ± 0.0066
		5.28	0.0205 ± 0.0045
		5.13	0.1243 ± 0.0050
		4.98	0.1002 ± 0.0050
J0005-0006	5.85	5.64	0.0823 ± 0.0069
		5.49	0.0718 ± 0.0070
		5.34	0.0961 ± 0.0066
		5.19	0.0578 ± 0.0063
		5.04	0.1567 ± 0.0073
J0818+1722	6.00	5.81	0.0216 ± 0.0053
		5.66	0.0440 ± 0.0040
		5.51	0.0984 ± 0.0043
		5.36	0.1192 ± 0.0039
		5.21	0.0884 ± 0.0039
		5.06	0.1285 ± 0.0042
J0836+0054	5.82	5.52	0.0907 ± 0.0011
		5.37	0.0348 ± 0.0009
		5.22	0.0606 ± 0.0009
		5.07	0.0751 ± 0.0011
		4.92	0.1276 ± 0.0011
J0840 + 5624	5.85	5.66	0.0883 ± 0.0176
		5.51	0.1127 ± 0.0260
		5.36	0.1661 ± 0.0202
		5.21	0.1191 ± 0.0167
		5.06	0.1765 ± 0.0190
J0927 + 2001	5.79	5.61	0.0884 ± 0.0136
		5.46	0.1041 ± 0.0163
		5.31	0.0596 ± 0.0104
		5.16	0.1165 ± 0.0105
		5.01	0.1268 ± 0.0117
J1030+0524	6.28	6.10	0.0012 ± 0.0010
		5.95	0.0060 ± 0.0010
		5.80	0.0260 ± 0.0012
		5.65	0.0462 ± 0.0009
		5.50	0.0661 ± 0.0009
		5.35	0.1147 ± 0.0008

Table 2. Ly α Transmitted Flux Ratio (continued)

Quasar	z_{em}	z_{abs}	T
J1044-0125	5.74	5.55	0.0686 ± 0.0022
		5.40	0.0520 ± 0.0020
		5.25	0.0427 ± 0.0019
		5.10	0.0898 ± 0.0020
		4.95	0.1139 ± 0.0022
J1048+4637	6.20	5.68	0.0117 ± 0.0011
		5.53	0.0519 ± 0.0012
		5.38	0.0736 ± 0.0011
J1137+3549	6.01	5.83	0.0116 ± 0.0029
		5.68	0.1010 ± 0.0024
		5.53	0.0742 ± 0.0026
		5.38	0.1341 ± 0.0022
		5.23	0.1323 ± 0.0023
		5.08	0.0530 ± 0.0025
J1148+5251	6.42	6.25	0.0015 ± 0.0005
		6.10	0.0051 ± 0.0005
		5.95	0.0038 ± 0.0005
		5.80	0.0186 ± 0.0006
		5.65	0.0433 ± 0.0005
		5.50	0.0278 ± 0.0005
J1250+3130	6.13	5.90	0.0108 ± 0.0033
		5.75	0.0055 ± 0.0030
		5.60	0.0248 ± 0.0026
		5.45	0.0077 ± 0.0026
		5.30	0.0776 ± 0.0024
J1306+0356	5.99	5.77	0.0645 ± 0.0020
		5.62	0.0690 ± 0.0016
		5.47	0.0991 ± 0.0015
		5.32	0.0864 ± 0.0014
		5.17	0.1156 ± 0.0013

Table 2. Ly α Transmitted Flux Ratio (continued)

Quasar	z_{em}	z_{abs}	T
J1335+3533	5.94	5.73	0.0224 ± 0.0059
		5.58	0.0445 ± 0.0074
		5.43	0.1215 ± 0.0083
		5.28	0.1217 ± 0.0058
		5.13	0.1293 ± 0.0064
J1411+1217	5.93	5.71	0.0322 ± 0.0033
		5.56	0.0665 ± 0.0031
		5.41	0.0858 ± 0.0029
		5.26	0.0690 ± 0.0028
		5.11	0.1650 ± 0.0030
J1436+5007	5.83	5.66	0.0714 ± 0.0217
		5.51	0.0775 ± 0.0315
		5.36	0.0895 ± 0.0239
		5.21	0.1292 ± 0.0199
		5.06	0.1509 ± 0.0224
J1602+4228	6.07	5.85	0.0687 ± 0.0057
		5.70	0.0729 ± 0.0044
		5.55	0.0795 ± 0.0058
		5.40	0.0802 ± 0.0055
		5.25	0.0934 ± 0.0036
J1623+3112	6.22	6.08	-0.0071 ± 0.0020
		5.93	0.0125 ± 0.0022
		5.78	0.0071 ± 0.0024
		5.63	0.0402 ± 0.0018
		5.48	0.0407 ± 0.0017
		5.33	0.0546 ± 0.0016
J1630+4012	6.05	5.77	-0.0165 ± 0.0342
		5.62	0.0495 ± 0.0323
		5.47	0.1015 ± 0.0353
		5.32	0.1376 ± 0.0296
		5.17	0.0869 ± 0.0219

Table 3. Ly β Transmitted Flux Ratio

Quasar	z_{em}	z_{abs}	${\mathcal T}$
J0002+2550	5.80	5.58	0.0557 ± 0.0039
J0005-0006	5.85	5.64	0.0786 ± 0.0066
J0818+1722	6.00	5.81	0.0341 ± 0.0035
J0840 + 5624	5.85	5.66	0.0898 ± 0.0127
J0927 + 2001	5.79	5.61	0.0715 ± 0.0088
J1030+0524	6.28	6.10	-0.0005 ± 0.0010
J1044-0125	5.74	5.55	0.0584 ± 0.0019
J1137 + 3549	6.01	5.83	0.0461 ± 0.0021
J1148 + 5251	6.42	6.25	0.0038 ± 0.0005
		6.10	0.0165 ± 0.0005
J1250 + 3130	6.13	5.90	0.0128 ± 0.0024
J1306+0356	5.99	5.77	0.0458 ± 0.0014
J1335 + 3533	5.94	5.73	0.0406 ± 0.0058
J1411+1217	5.93	5.71	0.0300 ± 0.0028
J1436 + 5007	5.83	5.66	0.0584 ± 0.0180
J1602+4228	6.07	5.85	0.0607 ± 0.0035
J1623 + 3112	6.22	6.08	-0.0036 ± 0.0019
		5.93	0.0305 ± 0.0017
J1630+4012	6.05	5.77	0.0499 ± 0.0194

This is the total observed transmission, without correcting for the foreground ${\rm Ly}\alpha$ absorption.

Table 4. Ly γ GP Optical Depth Measurements

object	z_{em}	redshift range	$\tau_{\rm GP}$ using Ly γ
J1030+0524	6.28	6.11 - 6.17	$> 14.2^1$
J1148 + 5251	6.42	6.25 - 6.32	14.7 ± 1.1
J1623 + 3112	6.22	6.05 - 6.15	> 12.2

1. 2- σ lower limit

Table 5. Evolution of Average GP Optical Depth and Dispersion

redshift range	$\langle \tau_{\mathrm{GP}} \rangle$	$\sigma(au_{ m GP})$
$4.90 - 5.15$ $5.15 - 5.35$ $5.35 - 5.55$ $5.55 - 5.75$ $5.75 - 5.95^{1}$ $5.95 - 6.25^{1}$	2.1 2.5 2.6 3.2 4.0 7.1	0.3 0.5 0.6 0.8 0.8

1. The redshift bin includes complete GP troughs, so the value is a lower limit

Table 6. Dark Troughs with $\Delta z > 0.1$ in the Highest-redshift Quasars

object	z_{em}	redshift range	$ au_{\mathrm{GP}}$ using $\mathrm{Ly} lpha$	$ au_{\mathrm{GP}}$ using $\mathrm{Ly}eta$
J1148+5251	6.42	6.10 - 6.32 $5.91 - 6.07$ $5.98 - 6.17$ $5.96 - 6.13$ $5.63 - 5.75$ $5.69 - 5.85$	6.2 ± 0.2	7.7 ± 0.2
J1148+5251	6.42		6.1 ± 0.2	5.5 ± 0.1
J1030+0524	6.28		$>6.3^{1}$	> 10.2
J1623+3112	6.22		>5.4	> 8.2
J1048+4637	6.20		>5.4	> 5.7
J1250+3130	6.13		>4.6	6.5 ± 0.6

1. 2- σ lower limit